Coupled thermal-hydraulic-mechanical-chemical modeling for permeability evolution of rocks through fracture generation and subsequent sealing

Sho Ogata*, Osaka University, Suita, 565-0871, JAPAN

Hideaki Yasuhara, Ehime University, Matsuyama, 790-8577, JAPAN

Naoki Kinoshita, Ehime University, Matsuyama, 790-8577, JAPAN

Kiyoshi Kishida, Kyoto University, Kyoto, 615-8530, JAPAN

*Corresponding author, E-mail address: ogatasyo97@gmail.com

Abstract

The coupled THMC model, *I*nterface for *P*ressure *S*olution *A*nalysis under *C*oupled *C*onditions, *IPSACC*, that was proposed by the authors and can describe the long-term evolution in rock permeability due to mineral reactions (i.e., pressure solution and free-face dissolution/precipitation) within rock fractures, was upgraded in the present study by incorporating the processes of fracture initiation/propagation. The remarkable characteristic of the proposed model is its ability to simulate the generation of fractures and the mineral reactions within the generated fractures as well as the subsequent changes in permeability. The proposed model was applied to predictions of the long-term changes in the permeability of rock located near high-level radioactive waste within a geological repository. The predicted results revealed that fractures were generated near the disposal cavity and that the permeability of the damaged zone increased significantly more than that of the intact rock during the excavation, while the permeability in almost the entire damaged zone decreased by about one order of magnitude due to pressure solution at the contacting asperities within the rock fractures after setting virtual radioactive waste into the disposal cavity. Overall, it was clarified that the proposed model is capable of calculating the permeability evolution of rock through fracture generation and subsequent sealing due to mineral reactions at the actual field scale. Thus, the potential for using the proposed model to examine the long-term performance of natural barriers for delaying the transport of radionuclides has been shown.

Key words: Coupled THMC process, rock permeability, pressure solution, fracture generation

1 Introduction

When securing the long-term performance of a geological disposal system for high-level radioactive waste (HLW), it is essential that the long-term evolution of the hydraulic property of the rock, that works as a natural barrier surrounding the radioactive waste, be evaluated. Within the surrounding rock, phenomena such as heat radiation from the waste package, mass transport with fluid flow, fracture initiation/propagation within rock masses due to the stress redistribution induced by the cavity excavation for disposing the radioactive waste, and the dissolution/precipitation of the minerals composing the rock, interact with each other complicatedly. These coupled interactions between the phenomena of the thermal, hydraulic, mechanical, and chemical components should bring about changes in the hydraulic property of the surrounding rock. Therefore, in order to evaluate the long-term evolution of the hydraulic property, it is necessary to conduct numerical analyses that can comprehensively consider the phenomena related to the thermal, hydraulic, mechanical, and chemical components and the interactions between these phenomena.

From previous works [1-8], it is well known that fracture initiation and propagation within rock masses during the excavation of a disposal cavity for radioactive waste will cause an increase in

54 permeability and a decrease in the stiffness and strength of the rock masses near the disposal cavity.
55 The area where these changes in the mechanical and hydraulic properties occur is called the
56 Excavation Damaged Zone (EDZ). In addition, mineral reactions of the free-face
57 dissolution/precipitation at the free surface and pressure solution at the contacting asperities within
58 rock fractures generated by the cavity excavation may occur and they may alter the rock permeability
59 with time [9, 10]. Other previous works [11-13] have shown that pressure solution at the contacting
60 asperities within fractures may change the permeability of the fractured rock by several orders of
61 magnitude over a long duration. Thus, it is necessary that a coupled model be developed that can
62 evaluate the geochemical reactions within rock fractures that may be newly generated by the cavity
63 excavation in order to predict the long-term evolution of the hydraulic property of natural barriers.
64 To date, several coupled thermal-hydraulic-mechanical-chemical (THMC) models have been
65 developed [14-19]. Some coupled models developed recently can consider the changes in the physical
66 properties such as the mechanical and hydraulic properties of rock masses due to fracture generation
67 [5, 20-25]. For example, Wei et al. [20] and Li et al. [21] developed a coupled thermal-hydraulic model
68 that can describe the fracture propagation by utilizing the damage theory, including the heterogeneity
69 of the mechanical property of the rock and the changes in the thermal property of the rock. They then
70 evaluated the evolution of the EDZ and the mechanical property of the rock under high-temperature
71 and high-confining pressure conditions. In addition, several coupled THMC numerical models that

consider the mineral dissolution/precipitation within rock fractures have been proposed in recent studies. For instance, Lang et al. [26] presented a discrete pore scale model that can describe the evolution of the fracture aperture due to pressure solution and elastic compression. Taron et al. [27] introduced a coupled THMC simulator, incorporating the strain due to the influence of mineral reactions, by linking TOUGHREACT and FLAC^{3D}. However, these coupled THMC models can simulate the mineral reactions and changes in the fracture geometry only on the existing fractures. [(Rev2.1.)] Although several coupled THMC models employing the damage theory include chemical phenomena between the rock mass and the fluid driven by the fracture generation [28, 29], they cannot consider the important process of pressure solution. Liu et al. [28] proposed a coupled THMC model taking into account the interaction between the chemical and damage components – the change in rock damage due to the change in the reaction rate of chemical erosion, and the change in the concentration of the fluidized solids from hydraulic and chemical erosion due to the change in the rock porosity brought about by the damage. Fan et al. [29] presented a coupled THMC process for acid fracturing within rock masses by considering the chemical reactions between the minerals and the acid enhanced by the increase in reaction sites due to the fracture initiation/propagation. As mentioned above, although coupled models have been developed, they cannot describe the processes of the mineral dissolution/precipitation including pressure solution and free-face dissolution/precipitation within the newly initiated and propagated fractures. [(Rev2.1)] Currently, therefore, it is difficult to predict the

changes in rock permeability over time in detail by the influence of the mineral reactions.

In this study, a coupled THMC model, denoted as the *I*nterface for *P*ressure *S*olution *A*nalysis under *C*oupled *C*onditions, *IPSACC*, is proposed by incorporating the damage theory and the processes of mineral dissolution/precipitation (i.e., pressure solution and free-face dissolution/precipitation) within the newly generated fractures. Then, the proposed model is applied to predict the long-term evolution of the rock permeability in geological disposal facilities containing high-level radioactive waste.

2 Numerical model

2.1 Model description

The coupled THMC model shown in this work can describe the interactions of the thermal, hydraulic, mechanical, and chemical processes (i.e., heat transfer from the waste package, the mass transport with the fluid flow, the fracture initiation/propagation within the rocks due to the stress redistribution induced by the cavity excavation for disposing radioactive waste, and the dissolution/precipitation of the rock minerals in pore water). Porous rock, working as a natural barrier, is set as the target of the calculation in this model; the physical phenomena in the artificial barrier are not considered. As shown in **Fig. 1**, the interactions of the multi-components were considered by adding the D (damage) component to the interactions between the T, H, M, and C components. The

model can describe the damage (fracture initiation/propagation) and the changes in the thermal, hydraulic, mechanical, and chemical properties of the rock due to the damage (expressed as gray arrows in **Fig. 1**), which were not considered in our previous model [19] (the interactions shown as white arrows in **Fig. 1** were taken into account in our previous model). In particular, being able to describe the mineral reactions within the generated fractures as well as the subsequent changes in permeability is the important characteristic of this upgraded model. Moreover, this model can even consider the mineral precipitation at the free-surface of the rock for multi-minerals, which was not possible with our previous model [19].

2.2 Governing equations

This model considers the groundwater flow, heat transfer, stress and deformation, fracture initiation/propagation, reactive transport, and mineral reactions. These phenomena are described by utilizing the governing equations, including the fluid flow equation of Darcy's law and the conservation law of water mass, the heat transfer equation, the poroelastic theory, the damage theory, the reactive transport equation, and the law of mineral reactions. In the following, the governing equations used in the proposed model are introduced.

(a) Stress analysis

In the mechanical process, assuming the plane strain condition, the stress distribution of the rock

structure is evaluated by the quasi-static equilibrium equation and the typical Hooke's law considering the changes in pore pressure and thermal stress based on the poroelastic theory, given by

$$-\nabla \cdot \boldsymbol{\sigma} = \boldsymbol{F}_v , \tag{1}$$

$$\boldsymbol{\sigma} = \boldsymbol{E} : (\boldsymbol{\varepsilon} - \boldsymbol{\alpha}_T \Delta T) + \alpha_B p \boldsymbol{I} , \tag{2}$$

where $\boldsymbol{\sigma}$ [Pa] is the stress tensor, $\boldsymbol{F}_v$ [Pa m^{-1}] is the body force, $\boldsymbol{E}$ [Pa] is the elasticity tensor, p [Pa] is the pore pressure, $\boldsymbol{\varepsilon}$ [-] is the strain tensor, $\boldsymbol{\alpha}_T$ [K^{-1}] is the thermal expansion coefficient of solid, T [K] is the temperature, α_B [-] is the Biot-Willis coefficient, and $\boldsymbol{I}$ [-] is the identity tensor.

(b) Damage theory

The isotropic damage theory is used for calculating the behavior of the rock fracture initiation and propagation. The damage theory defines a fracture as not discontinuous deformation, but as the decrease in stiffness of the continuum. As this theory can consider the fracture as a continuum, it is compatible with the FEM and has high versatility and extensibility. Thus, it has been used in a number of calculations for fracture initiation/propagation [20-23, 30-35]. In the current model, the damage evolution law proposed previously by Tang (1997) [30] and Zhu and Tang (2004) [32] is utilized. The stress-strain relation of an element under the conditions of uniaxial tension and uniaxial compression can be described as the function shown in **Fig. 2**. Damage induced by tension or shear occurs when

140 the stress state satisfies the maximum tensile stress criterion or the Mohr-Coulomb failure criterion,

141 respectively, as expressed by

142 $$\begin{cases} F_1 \equiv \sigma_3 + f_{t0} = 0 \\ F_2 \equiv \sigma_1 - \dfrac{1+\sin\theta}{1-\sin\theta}\sigma_3 - f_{c0} = 0 \end{cases}, \quad (3)$$

143 where F_1 and F_2 are the two damage threshold functions for tensile damage and shear damage,

144 respectively, σ_1 [Pa] and σ_3 [Pa] are the maximum and minimum principal stresses, respectively, f_{t0}

145 [Pa] and f_{c0} [Pa] are the uniaxial tensile strength and uniaxial compressive strength, respectively, and

146 θ [rad] is the internal friction angle. In this work, the tensile stress and the compressive stress are set

147 to be negative stress and positive stress, respectively.

148 In the isotropic damage theory, the elastic modulus E of the damaged rock monotonically decreases

149 with the evolution of damage, given as

150 $$E = (1 - D) E_0, \quad (4)$$

151 where E_0 [Pa] and E [Pa] are the elastic modulus of the rock before and after the initiation of damage,

152 respectively, and D [-] is the scalar damage variable that varies from 0 to 1.0 and represents the degree

153 of damage to the targeted material. D becomes 0 when damage does not occur and 1 when complete

154 damage occurs. In a damage model, the damaged zone ($D > 0$) can be assumed as a mesoscopic fracture

155 [33]. In general, a macroscopic fracture formed by the calescence of multiple mesoscopic fractures is

156 called a “fracture”. In the current work, however, a mesoscopic fracture (a damaged zone : $D > 0$) is

157 defined as a “fracture”. Damage variable *D* is evaluated by strain as follows [31]. In the linear elastic

158 law, principle stress σ_i is expressed by the principle strain and the volumetric strain, as follows:

159 $$\sigma_i = \frac{E}{1+\nu}\left[\varepsilon_i + \frac{\nu}{1-2\nu}\varepsilon_v\right], \tag{5}$$

160 where ε_i (i = 1, 2, 3) are the principle strains in the first, second, and third principal stress directions,

161 respectively, ε_v [-] is the volumetric strain, and ν [-] is Poisson’s ratio. Based on Eq. (5), the strains

162 of ε_t and ε_c, which are used to calculate damage variable *D*, are expressed by the following

163 equations:

164 $$\bar{\varepsilon}_1 = \frac{1}{1+\nu}\left[\varepsilon_1 + \frac{\nu}{1-2\nu}\varepsilon_v\right], \tag{6}$$

165 $$\bar{\varepsilon}_3 = \frac{1}{1+\nu}\left[\varepsilon_3 + \frac{\nu}{1-2\nu}\varepsilon_v\right] = \varepsilon_t, \tag{7}$$

166 $$\varepsilon_c = \bar{\varepsilon}_1 - \frac{1+\sin\theta}{1-\sin\theta}\bar{\varepsilon}_3, \tag{8}$$

167 According to the failure criteria of Eq. (3) and the constitutive law shown in **Fig. 2**, damage variable

168 *D* is calculated as follows:

169 $$D = \begin{cases} 0 & F_1 < 0 \text{ and } F_2 < 0 \\ 1 - \left|\dfrac{\varepsilon_{t0}}{\varepsilon_t}\right|^{\eta} & F_1 = 0 \quad \text{and} \quad \Delta F_1 > 0 \\ 1 - \left|\dfrac{\varepsilon_{c0}}{\varepsilon_c}\right|^{\eta} & F_2 = 0 \quad \text{and} \quad \Delta F_2 > 0 \end{cases}, \tag{9}$$

170 where ε_{t0} [-] and ε_{c0} [-] are the limit tensile and compressive strain, respectively, and η [-] is the

171 constant ($\eta = 2$). In Eq. (9), F_1 and $\Delta F_1 > 0$ express the rock damage in the tensile mode when its

172 stress state satisfies the maximum stress criterion and the rock is still under a loading condition.

Similarly, F_2 and $\Delta F_2 > 0$ express the damage in the shear mode when its stress state satisfies the Mohr-Coulomb criterion and the rock is still under a loading condition. Damage variable D is an important parameter for calculating the changes in the physical properties of the rock.

(c) Heterogeneity of mechanical properties

In the model, in order to describe the heterogeneity of the rock, local mechanical properties within the rock mass are set by statistical dispersion based on the Weibull distribution [36]. The mechanical properties of all the elements in the calculation domains are assumed to follow the given Weibull distribution. Among the mechanical properties, the heterogeneity of Poisson's ratio is the lowest. Although the ratio is set homogeneously, the elastic modulus, uniaxial tensile strength, and uniaxial compressive strength are defined by the following probability density function [20-23, 30-35]:

$$f(u) = \frac{m}{u^s}\left(\frac{u}{u^s}\right)^{m-1} \exp\left[-\left(\frac{u}{u^s}\right)^m\right], \tag{10}$$

where u is the mechanical parameter of each element in the calculation domain, such as the strength and the elastic modulus (i.e., $u = E_0$, f_{t0}, and f_{c0}), u^s is the scale parameter which is related to the average value of the mechanical parameter, u (i.e., $u^s = E_0^s$, $f_{t0}{}^s$, and $f_{c0}{}^s$), and m [-] is the homogeneity index of the material properties which describe the shape of the distribution function.

(d) Fluid flow

The groundwater flow in the rock is calculated by the conservation of water mass based on the poroelastic theory and by assuming the Darcian flow, as follows:

$$\rho_w S \frac{\partial p}{\partial t} + \nabla \cdot (\rho_w \boldsymbol{u}) + \rho_w \alpha_B \frac{\partial \varepsilon_v}{\partial t} = f_w, \tag{11}$$

$$\boldsymbol{u} = -\frac{\boldsymbol{k}}{\mu}(\nabla p + \rho_w g \nabla h), \tag{12}$$

where ρ_w [kg m^{-3}] is the density of the fluid, S [Pa^{-1}] is the storage coefficient, $\boldsymbol{u}$ [m s^{-1}] is the fluid velocity tensor, f_m [kg m^{-3} s^{-1}] is the source term for the flow, $\boldsymbol{k}$ [m^2] is the rock permeability tensor, μ [Pa s] is the fluid dynamic viscosity, g [m s^{-2}] is the gravity acceleration, and h [m] is the potential head. The permeability within the undamaged and damaged zones is expressed as

$$k = \begin{cases} k_0 & D = 0 \\ \dfrac{b^2}{12} & D > 0 \end{cases}, \tag{13}$$

where k_0 [m^2] is the permeability of the undamaged rock and b [m] is the average fracture aperture. Within the damaged zone, it is assumed that three orthogonal plane fractures have formed, as shown in **Fig. 3**. The changes in rock permeability and fracture aperture due to the evolution of damage are represented as [37]

$$k_D = k_0 \exp(\alpha_k D), \tag{14}$$

$$b_D = \sqrt{12 k_D} = \sqrt{12 k_0 \exp(\alpha_k D)}, \tag{15}$$

where k_D [m^2] is the permeability of the damaged rock, α_k [-] is the coefficient that represents the damage-permeability effect, and b_D [m] is the fracture aperture of the damaged rock.

(e) Heat transfer

In the thermal process, the temperature of the rock is calculated by the following heat transfer equations:

$$(\rho C_p)_{eq}\frac{\partial T}{\partial t}T = \nabla\cdot(\boldsymbol{\lambda_{eq}}\nabla T) - \rho_w C_{p,w}\boldsymbol{u}\cdot\nabla T + q_h, \tag{16}$$

$$(\rho C_p)_{eq} = (1-\varphi)\rho_m C_{p,m} + \varphi\rho_w C_{p,w}, \tag{17}$$

where $(\rho C_p)_{eq}$ [J K^{-1} m^{-3}] is the equilibrium volumetric heat capacity, $C_{p,w}$ [J kg^{-1} K^{-1}] is the heat capacity of the fluid, $\boldsymbol{\lambda_{eq}}$ [W m^{-1} K^{-1}] is the equilibrium thermal conductivity tensor, q_h [W m^{-3}] is the heat source, ρ_m [kg m^{-3}] is the density of the solid, $C_{p,m}$ [J kg^{-1} K^{-1}] is the heat capacity of the solid, and φ [-] is the porosity. When referring to Zimmerman (1989) [38], the equilibrium thermal conductivity is expressed by the known Hashin-Shtrikman upper bound [39] by assuming that the targeted media have spherical pores, as

$$\boldsymbol{\lambda_{eq}} = \boldsymbol{\lambda_m} + \frac{3\boldsymbol{\lambda_m}(\boldsymbol{\lambda_w}-\boldsymbol{\lambda_m})\varphi}{3\boldsymbol{\lambda_m}+(\boldsymbol{\lambda_w}-\boldsymbol{\lambda_m})(1-\varphi)}, \tag{18}$$

where $\boldsymbol{\lambda_m}$ and $\boldsymbol{\lambda_w}$ [W m^{-1} K^{-1}] are the thermal conductivity tensors of the solid and the fluid, respectively.

220 In the model, the change in thermal conductivity due to the evolution of damage is assumed as [33]

221 $$\lambda_m = \begin{cases} \dfrac{\lambda_{m0}}{0.99 + T(C_a - C_b / \lambda_{m0})} & D < 1 \\ \xi \lambda_{m0} & D = 1 \end{cases} \quad (19)$$

222 where λ_{m0} [W m^{-1} K^{-1}] is the initial thermal conductivity of the solid without the effect of either
223 temperature or damage, C_a [-] and C_b [-] are empirical constants derived from the experimental results
224 [40] (the constants for crystalline rocks are $C_a = 0.0030 \pm 0.0015$ and $C_b = 0.0042 \pm 0.0006$; the
225 corresponding coefficients for sedimentary rocks are $C_a = 0.0034 \pm 0.006$ and $C_b = 0.0039 \pm 0.0014$),
226 and ξ ($\xi < 1$) is the coefficient representing the effect of the damage on the thermal conductivity (ξ is
227 the ratio of the thermal conductivity of the solid to the fluid, $\xi = \lambda_w / \lambda_{m0}$).

228 **(f) Reactive transport**

229 The solute transport behavior in the pore water is calculated by the basic advection-diffusion
230 equation. In the proposed model, the mechanical dispersion and the retardation due to the sorption
231 processes are not considered.

232 $$\frac{\partial (c_i \phi)}{\partial t} = \nabla \cdot (\boldsymbol{D}_{e,i} \nabla c_i) - \boldsymbol{u} \cdot \nabla c_i + r_i \,, \quad (20)$$

233 $$\boldsymbol{D}_{e,i} = \phi \tau \, \boldsymbol{D}_{b,i} \,, \quad (21)$$

234 $$r_i = \sum_j^n \nu_i R_j \,, \quad (22)$$

where c_i [mol m^{-3}] is the concentration of solute i in the pore water, $\boldsymbol{D_{e,i}}$ [m^2 s^{-1}] is the effective diffusion coefficient tensor, $\boldsymbol{D_{b,i}}$ [m^2 s^{-1}] is the diffusion coefficient tensor, τ [-] is the coefficient related to tortuosity (τ = 1.0), r_i [mol m^{-3} s^{-1}] is the source term of solute i, where v_i [-] is the stoichiometry coefficient of solute i in the pore water, n is the number of minerals composing the targeted rock, and R_j [mol m^{-3} s^{-1}] is the rate of the mineral reactions for mineral j. The dissolution rate constant and diffusion coefficient are temperature-dependent and can be defined by an Arrhenius-type equation [41].

$$D_{b,i} = D_{b,i}^{0} \exp(-E_{D,i} / RT) , \tag{23}$$

where $D_{b,i}^{0}$ [m^2 s^{-1}] and $E_{D,i}$ [J mol^{-1}] are the pre-exponential factor and the activation energy of the diffusion of solute i, respectively, and R [J mol^{-1}K^{-1}] is the gas constant.

(g) Pressure solution within fractures

In the current work, the mineral reactions include the mineral dissolution/precipitation on the free-surface within the rock fractures and the mineral dissolution at the contacting asperities within the rock fractures (pressure solution). Thus, the rate of the mineral reactions for mineral j, R_j, is expressed by

$$R_j = R_j^{FF} + R_j^{PS} , \tag{24}$$

where R_j^{FF} [mol m^{-3} s^{-1}] is the rate of the free-face dissolution/precipitation of mineral *j* within the rock fracture, and R_j^{PS} [mol m^{-3} s^{-1}] is the rate of the pressure solution of mineral *j* at the contacting asperities within the rock fracture.

Within rock fractures, pressure solution may occur at the contacting asperities (fracture contacts). When pressure solution occurs continuously at the fracture contacts, fracture aperture *b* decreases and the fracture contact area increases with time. As shown in **Fig. 4**, when the geometric model obtained by idealizing the arbitrary micro-domain, composed of contacting asperities and pore space, is set as the representative element of the rock fractures [11], the rate of the pressure solution of mineral *j* at the contacting asperities within the rock fracture, defined by Ogata et al. [19], is given as follows:

$$R_j^{PS} = \frac{3 f_r \chi_j R_c V_{m,j} k_{+,j}}{RTb(1-R_c)} \cdot \left(\frac{\sigma'_m}{R_c} - \sigma_c \right), \tag{25}$$

$$R_c = \frac{A_t^c}{A_t^l}, \tag{26}$$

where $k_{+,j}$ [mol m^{-2} s^{-1}] is the mineral dissolution rate constant of mineral *j*, χ_j [-] is the volumetric ratio of mineral *j*, R_c [-] is the contact-area ratio within the fracture, $V_{m,j}$ [m^3 mol^{-1}] is the molar volume of mineral *j*, f_r [-] is the roughness factor, which is the ratio of the true (microscopic) surface area over the apparent (geometric) surface area, σ'_m [Pa] is the mean effective stress, σ_c [pa] is the critical stress, A_t^l [m^2] is the total fracture cross-sectional area in the representative element, and A_c^l [m^2] is the contact area within the fracture of the representative element, $A_c^l = R_c A_t^l$. The mineral dissolution rate constants are defined by the Arrhenius expression, given as

$$k_{+,j} = k^0_{+,j} \exp(-E_{k_{+,j}} / RT), \tag{27}$$

where k^0_{+j} [mol m^{-2} s^{-1}] is the pre-exponential factor of mineral *j* and $E_{k_{+,j}}$ [J mol^{-1}] is the activation energy of the dissolution of mineral *j*.

The occurrence of pressure solution induced by the generated fractures is formulated based on Eq. (25). In the proposed model, a fracture is generated when $D > 0$. Therefore, the free-face dissolution and pressure solution within fractures occur only in the damaged zone where $D > 0$. In addition, Eq. (25) can be extended by considering the failure mode of fractures. To date, the component of stress that works as the driving force of pressure solution in a multi-dimensional space has not been clearly established. Some previous studies have implied that pressure solution is related to plastic or brittle deformation in the contact-area (e.g., Tada and Silver (1987) [42]). Thus, in this work, the differential stress between the principal stresses that work as the driving force of the rock failure and the pore pressure is assumed as the driving force of pressure solution at the contacting asperities within the fracture after any damage has been generated.

Consequently, the rate of pressure solution is expressed by considering damage variable *D* and the failure modes of the fracture, F_1 and F_2 (Eq. (3)), given as follows:

$$\begin{cases} R_j^{PS} = 0 & D = 0 \\ R_j^{PS} = \dfrac{3R_c f_r \chi_j V_{m,j} k_{+,j}}{RTb \quad (1-R_c)} \left(\dfrac{\langle \sigma'_3 \rangle}{R_c} - \sigma_c \right) & D > 0, F_1 = 0 \\ R_j^{PS} = \dfrac{3R_c f_r \chi_j V_{m,j} k_{+,j}}{RTb \quad (1-R_c)} \left(\dfrac{\langle \sigma'_1 \rangle + \langle \sigma'_3 \rangle}{R_c} - \sigma_c \right) & D > 0, F_2 = 0 \end{cases}, \tag{28}$$

where <> represents the following function:

$$\langle x \rangle = \begin{cases} x & x \geq 0 \\ 0 & x < 0 \end{cases}. \quad (29)$$

The proposed model assumes that the directions of the principal stresses do not change with time after the termination of the fracture initiation/propagation. Thus, the influence of the changes in the directions of the principal stresses after the fracture initiation/propagation on the pressure solution is not considered.

(h) Free-face dissolution/precipitation within fractures

The rate of the free-face dissolution within rock fractures has been defined by Ogata et al. [19] as follows:

$$R_j^{FF} = 2 f_r \chi_j k_{j,+} (1 - Q_j / K_{eq,j}) / b, \quad (30)$$

where Q_j [-] is the ionic activity product and $K_{eq,j}$ [-] is the equilibrium constant of mineral j. When $Q_j / K_{eq,j} < 1$, free-face dissolution occurs, and when $Q_j / K_{eq,j} > 1$, free-face precipitation occurs.

As a fracture is generated when $D > 0$ in the proposed model, the rate of the free-face dissolution/precipitation is defined as

$$\begin{cases} R_j^{FF} = 0 & D = 0 \\ R_j^{FF} = 2 f_r \chi_j k_{+,j} (1 - Q_j / K_{eq,j}) / b & D > 0 \end{cases}. \quad (31)$$

(i) Fracture aperture change

In the current work, only the change in the fracture aperture is considered in the calculation; the change in the porosity within the rock matrix is not considered. The change in the fracture aperture is induced by the fracture initiation/propagation and mineral dissolution/precipitation. Thus, the fracture aperture at arbitrary time t is defined by considering the aperture generated by the fracture initiation/propagation and the temporal alternation of the aperture due to the free-face dissolution/precipitation and pressure solution, as

$$b(t) = b_D + \int \dot{b}^{FF}(t)dt + \int \dot{b}^{PS}(t)dt \,, \tag{32}$$

$$\dot{b}^{FF} = \sum_{j}^{n} 2 f_{r,j} \chi_j (1 - R_c) V_{m,j} k_{+,j} (1 - Q_j / K_{eq,j}) \tag{33}$$

$$\begin{cases} \dot{b}^{PS}(t) = \sum_{j}^{n} \dfrac{-3 f_r \chi_j k_{+,j} V_{m,j}^2}{RT} \left(\dfrac{\langle \sigma'_3 \rangle}{R_c} - \sigma_c \right) & D > 0, F_1 = 0 \\ \dot{b}^{PS}(t) = \sum_{j}^{n} \dfrac{-3 f_r \chi_j k_{+,j} V_{m,j}^2}{RT} \left(\dfrac{\langle \sigma'_1 \rangle + \langle \sigma'_3 \rangle}{R_c} - \sigma_c \right) & D > 0, F_2 = 0 \end{cases} , \tag{34}$$

where $\dot{b}^{FF}$ [m s^{-1}] is the rate of change in the fracture aperture by free-face dissolution/precipitation and $\dot{b}^{PS}$ [m s^{-1}] is the rate of change in the fracture aperture by pressure solution. Mineral reactions alter the fracture aperture, and the contact-area ratio within the fractures changes due to the change in the fracture aperture. The relation between the fracture aperture and the contact-area ratio within the fractures may be given by the following simple equation [12]:

$$b(t) = b_r + (b_D - b_r) \exp(-(R_c(t) - R_{cD}) / a) \,, \tag{35}$$

where b_r [m] is the residual fracture aperture, R_c (t) [-] is the contact-area ratio within the fracture at

arbitrary time t, R_{cD} [-] is the contact-area ratio within the fracture when a fracture is generated, and a [-] is a constant.

(j) Relation between fracture initiation/propagation and contact area ratio with change in fracture aperture

The contact-area ratio within the fracture when a fracture is generated, given in Eq. (35), is explained in detail. Based on the continuum damage theory, damage variable D is defined as the ratio of the arbitrary cross-sectional area of the representative element over the pore space of the representative element [43]. In the proposed model, the arbitrary domain composed of contacting asperities and pore space, is assumed as the representative element of the rock fractures. Therefore, the contact-area ratio within the fracture, when a fracture is generated, R_{cD}, is represented using damage variable D of the representative element of the rock fractures, given as

$$D = \frac{A_t^l (1 - R_{cD})}{A_t^l}, \tag{36}$$

$$R_{cD} = 1 - D. \tag{37}$$

In the current work, after the fracture initiation/propagation, changes in damage variable D are not considered.

2.2 Numerical implementation

The calculation procedure for the proposed model is shown in **Fig. 5**. As shown in this figure, the proposed model is solved by using two numerical tools of COMSOL MULTIPHYSICS [44], namely, simulation software using the Finite Element Method (FEM), and PHREEQC [45], a geochemical code that enables the calculation of various geochemical reactions for multi-minerals based on abundant thermo-dynamic databases. The interface between COMSOL and PHREEQC that controls the calculation procedure (**Fig. 5**) is linked by MATLAB language. In the calculation scheme, the reactive transport process (Eq. (20)) is divided into two parts by applying a non-iterative sequential split operator approach [46] - one part is the solute transport by advection and diffusion, and the other part comprises the mineral reactions. The model is calculated according to the following steps:

(1) In the beginning of the whole process, the fracture initiation and propagation within the rock under the given boundary conditions of stress and deformation are calculated by a damage analysis using the damage theory. This process is implemented in COMSOL by applying the calculation steps based on the steady-state analysis. The stress distribution, when completing the damage analysis, is set as the initial condition for subsequent time-dependent analyses. In the same way, other variables given by damage analysis – damage variable D and the physical properties of rock, that depend on D (i.e., elastic modulus, permeability, fracture aperture, thermal conductivity, and contact-area ratio within the

fracture – see Eqs. (4), (13), (15), (19), and (37)), are utilized to define the fracture distribution and the initial material properties for the next calculation process.

(2) At the beginning of the subsequent time-dependent process, the solute transport step (see Eq. (38)) in a time step Δt is solved with other coupled THM processes using COMSOL.

$$\frac{\partial(c_i^k \phi)}{\partial t} = \nabla \cdot (\boldsymbol{D}_{e,i} \nabla c_i^k) - \boldsymbol{u} \cdot \nabla c_i^k , \tag{38}$$

where c_i^k [mol m^{-3}] is the concentration of solute i in the pore water calculated by the solute transport step.

(3) Then, selected variables for the concentrations of each solute, temperature, fracture aperture, the contact-area ratio within the fracture, the rate of the pressure solution of each mineral, the rate of change in fracture aperture by pressure solution at each finite element mesh node in the damaged area ($D > 0$) are outputted to PHREEQC. In the proposed model, mineral reactions occur only within the damaged area. Thus, the calculation of the mineral reactions by PHREEQC is performed for node points within the damaged area. The temperature, fracture aperture, and contact-area ratio within the fracture are used to define the rate of the free-face dissolution/precipitation and the rate of change in the fracture aperture by the free-face dissolution/precipitation for each mineral (Eqs. (31) and (33)) in PHREEQC. Through the calculation by PHREEQC, the updated concentrations of each solute due to the mineral reactions of the free-face dissolution/precipitation and pressure solution at each finite element mesh node in the damaged area in time step Δt are given as follows:

$$c_i^{k+1} = c_i^k + r_i \Delta t \,, \tag{39}$$

where c_i^{k+1} [mol m^{-3}] is the concentration of solute i in the pore water, updated by the process of mineral reactions. Moreover, the updated fracture aperture and permeability are also calculated. Subsequently, these variables obtained from PHREEQC at all the mesh nodes within the damaged area are set as the initial values of the calculation by COMSOL in the next time step.

The time-dependent coupled THMC processes are solved by repeating the above-mentioned steps (2)-(3).

3 Model verification

In the following, some benchmark simulations are conducted in order to verify the basic performance of the proposed model.

3.1 Coupled THM process

The thermal pressurization problem solved by Coussy (2004) [47] is selected as a benchmark simulation for the coupled THM process. The model geometry and the initial/boundary conditions utilized in the simulation are shown in **Fig. 6**. The calculation domain, which has a length of 15.0 m and a width of 1.0 m, is discretized into 40×600 (24000) square elements. In the initial state, the pore pressure, temperature, and displacement are all equal to zero. On the top boundary, temperature T_b =

386 50°C is applied, and the border is set to be drained and free of stress. Under these initial/boundary

387 conditions, analytical solutions for the non-dimensional temperature and pore pressure are derived by

388 Coussy (2004) [47], as follows:

389 $$\overline{T} = \frac{T}{T_b} = 1 - erfc\left(\frac{y}{2\sqrt{c_T t}}\right) \tag{40}$$

390 $$\overline{p} = \frac{p}{c_f T_b \frac{\omega}{k}\mu} = \left(1 - \frac{c_f}{c_T}\right)^{-1}\left[erfc\left(\frac{y}{2\sqrt{c_f t}}\right) - erfc\left(\frac{y}{2\sqrt{c_T t}}\right)\right] \tag{41}$$

391 $$\omega = \frac{3\alpha_T K \alpha_B}{K + \frac{4}{3}G} - 3\alpha_m \tag{42}$$

392 $$c_f = \frac{k}{S\mu}\frac{\left(K + \frac{4}{3}G\right)}{\left(K_u + \frac{4}{3}G\right)} \tag{43}$$

393 $$c_T = \frac{\lambda_{eq}}{(\rho C_p)_{eq}} \tag{44}$$

394 where $\overline{T}$ and $\overline{p}$ are the non-dimensional temperature and pore pressure, respectively, y [m] is the

395 depth from the top boundary, c_T [m^2 s^{-1}] is the heat diffusion coefficient, c_f [m^2 s^{-1}] is the fluid

396 diffusion coefficient, K [Pa] is the bulk modulus, $K_u = K + \alpha_B^2 / S$ is the undrained bulk modulus, G

397 [Pa] is the shear modulus, and α_m [K^{-1}] is the coefficient of total thermal expansion. The parameters

398 used in the simulation are summarized in **Table 1**. Comparisons of the simulation results by the current

399 model and the analytical solutions (Coussy, 2004) [47] for the distribution of non-dimensional

400 temperature and non-dimensional pore pressure at different depths and at various times (t = 1.0 ×10^6,

401 5.0 ×10^6, and 1.0 ×10^7 s) are depicted in **Figs. 7 (a) and (b)**. These figures show that all the simulation

results are in excellent agreement with the analytical solutions and that the proposed model can describe the theoretical response of coupled THM problems accurately.

3.2 Reactive transport process

Subsequently, the accuracy of the implementation of the reactive transport process is verified. In particular, the correctness of the linking between the transport solver (COMSOL) and the geochemical reaction solver (PHREEQC) by MATLAB for describing the total reactive transport process is investigated. As shown in **Fig. 8**, the 1D reactive transport problem performed by Nardi et al. (2014) [48] is solved as the benchmark. The calculation domain, composed of 160 nodes, is fully saturated under the isothermal condition. In the domain, the velocity and the diffusion coefficient within the pore water are set to be 2.78×10^{-6} m/s and 5.55×10^{-9} m^2/s , respectively. The concentration of chemical solutes in the domain is altered with time by the interaction between the inflow water from the inlet and the multi-minerals contained in the domain (illite, k-feldspar, albite, pyrite, and calcite). All the minerals, except for the calcite, employ kinetic dissolution, and the calcite is in equilibrium with the initial water composition. The chemical conditions (compositions of the chemical solutes/minerals and pH) of the calculation domain at the initial state and the inlet boundary used in the benchmark simulation are summarized in **Table 2**. All the parameters and formulas for the kinetic dissolution used here are equivalent to those of the PHREEQC source code by Nardi et al. (2014) [48]. Comparisons

420 of the results by the proposed model and the PHREEQC solution for the concentrations of Al and K
421 observed at the outlet boundary are shown in **Figs. 9 (a) and (b), respectively**. As is apparent from
422 the figures, the profiles for the concentrations of both Al and K coincide well with the solutions derived
423 by PHREEQC alone, and they imply the correctness of the numerical implementation in the reactive
424 transport process, including the link between COMSOL and PHREEQC by MATLAB.

425 # 4 Numerical analyses for long-term prediction

426 The proposed model was also applied to predict the long-term evolution of the permeability in
427 rock located near high-level radioactive waste within a geological disposal system. In the following
428 predictions, the subsurface environment was modeled by referring to the Horonobe area of Hokkaido,
429 Japan and the actual data were obtained from related literature. In the analysis, the horizontal storage
430 of radioactive waste, as shown in the scientific and technical report summarizing the HLW disposal
431 construction in Japan [49], was assumed. As shown in **Fig. 10**, bedrock from depths of 325 m to 375
432 m from the ground surface, with a disposal cavity at a depth of 350 m, was set as the calculation
433 domain [1]. The calculation domain was discretized into 82184 triangular elements. The canisters of
434 radioactive waste were virtually installed in the cavity as a heat source. The horizontal length of the
435 calculation domain was 50.0 m. The target for the calculation was set to be siliceous mudstone with a
436 porosity 41.6% and a dry density of 1420 kg/m^3 [1]. These physical properties were obtained from in-

situ experiments conducted in the gallery at a depth of 350 m by the Horonobe Underground Research Center of the Japan Atomic Energy Agency (JAEA) [1]. With regard to the mechanical properties, the elastic modulus and each type of strength (uniaxial tensile strength and uniaxial compressive strength) were distributed within the domain by the Weibull distribution and the other properties were set homogeneously. The hydraulic and thermal gradients were set to be 1/1000 and 5°C/100 m, respectively [50]. In this analysis, at first, a simulation of the cavity excavation was conducted. Secondly, by setting the stress condition obtained from the excavation analysis as the initial condition, the long-term prediction of the changes in permeability was conducted. It should be noted that although the simulation of the cavity excavation was relatively simple compared to the real in-situ construction process of a geological repository, the assumed subsurface conditions (e.g., the initial stress conditions, the material properties of the rock, and the chemical conditions, including the pH and the mineral compositions) may conform to those of the actual field. Therefore, the trend of the evolution of the physical/chemical behavior of the rock at the targeted site during the period of geological disposal can be captured by the following analyses.

4.1 Analysis of cavity excavation

In the analysis of the cavity excavation, as shown in **Fig. 10**, the mechanical behavior of the rock was evaluated, including the fracture evolution during the excavation of the disposal cavity with a

diameter of 2.0 m and a depth of 350 m. The characteristic values for the distributions of the mechanical properties that conform to the Weibull distribution, namely, $f_{t0}{}^{s}$, $f_{c0}{}^{s}$, and $E_0{}^{s}$, (see Eq. (10), were set to be 1.83 MPa, 15.4 MPa, and 1.82 GPa, respectively. These values are equivalent to the average values of the mechanical properties obtained from the laboratory tests conducted with rock cores collected from a borehole drilled at a depth of 350 m [1]. Based on previous studies [32, 34], it was suggested that homogeneity index m (see Eq. (10)) be in the range of 1.2 ~ 5.0 for accurately simulating the fracture process within the rock. With reference to these literary references, homogeneity index m was set to be 3.0. Poisson's ratio and the internal friction angle were set to be 0.17 [1] and 30° [51], respectively. Confining stresses of 5.08 MPa and 4.84 MPa were imposed at the top and side boundaries, respectively (**Fig. 11**). These initial stress conditions were estimated by Aoyagi and Ishii (2018) [1] based on hydraulic fracturing tests conducted at the target site and in the 350-m gallery [52]. The initial pore pressure at a depth of 350 m corresponds to the measured value at the equivalent depth in the boreholes installed at the target site [1]. The excavation analysis of this work assumed a short-term excavation [1]. In this situation, it is assumed that the excavated wall is in an undrained condition during the excavation. Thus, the mechanical stress/deformation and damage were calculated without hydro-mechanical coupling. In this analysis, firstly, the internal outward radial pressure applied to the cavity boundary to replace the in-situ stress condition is evaluated, and then it decreases monotonically by 1% per step for 100 steps (**Fig. 11**). The evolution of the fracture

initiation/propagation (change in distribution of damage variable D) around the cavity during the excavation is shown in **Fig. 12**. In this figure, in order to distinctly display the two kinds of damage modes (i.e., tensile damage and shear damage), the sign of the damage variable D values in the shear damage is changed to negative (i.e., $0 \leq D \leq 1 \Rightarrow -1 \leq D \leq 0$). Therefore, the shear damage (areas in red) is represented with negative numbers ($-1 \leq D < 0$), while the tensile damage (areas in blue) is represented with positive ones ($0 < D \leq 1$). As is apparent from the figure, a number of fractures were generated around the periphery of the cavity and the shear damage is more remarkable than the tensile damage. The tensile damage occurs near the shear damage. This is likely to be because the compressive deformation is enhanced by the decrease in the elastic modulus due to the evolution of shear damage, and tensile stress occurs within the surrounding rock (rock near the shear damage zone), which may result in the pulling of the neighboring shear damage.

4.2 Long-term coupled THMC analysis

The physical properties of rock that depend on damage variable D (i.e., elastic modulus, permeability, fracture aperture, thermal conductivity, and contact-area ratio within the fracture), and were calculated by the excavation analysis, are set as the initial conditions. Then, the coupled THMC numerical analysis was conducted. The analysis period was set to be 10^2 years after the disposal of the waste package in the excavated cavity.

In this analysis, the rock used for the calculations was assumed to be fully saturated with water and to be composed of six minerals, namely, quartz, k-feldspar, albite, anorthite, smectite, and cristobalite. The volumetric ratios of composing minerals χ_j are listed in **Table 3**. These mineral compositions were set by referring to those obtained from the gallery at a depth of 350 m at the target site [53], but the opal-CT contained in the mudstone was replaced with cristobalite whose chemical properties are almost similar to those of opal-CT. The concentrations of seven chemical solutes (Si, Na, K, Ca, Al, Mg, and Fe), contained in the above forming minerals, were considered in the reactive transport process. The parameters of the kinetic dissolution rate constants for the minerals considered in the calculations are summarized in **Table 4**. The important parameters of the dissolution rate constants for the six minerals used in Eq. (27), which depend on the temperature, were obtained from the literature [54-59].

In this analysis, the heat source from the radioactive waste was considered by setting the time-dependent temperature T_b(t) outside the buffer material obtained from the literature [49] (**Fig. 13**) at the periphery of the cavity as the boundary conditions. A description of the long-term coupled THMC analysis, including the boundary/initial conditions, is given in **Fig. 14**. In the calculation of the heat transfer, the following Neumann boundary condition is set at all the boundaries excluding the periphery of the cavity:

$$\frac{\partial T}{\partial \boldsymbol{n}} = 0 \,, \tag{39}$$

where $\boldsymbol{n}$ represents the outward normal direction to the targeted boundary. In the calculation of the reactive transport, the following Neumann boundary condition is set at all the boundaries.

$$\frac{\partial c_i}{\partial \boldsymbol{n}} = 0 . \tag{40}$$

The concentrations of each chemical solute in the pore water at the average temperature of the whole domain at the initial state (i.e., 32.5 °C) and the pH value measured at a depth of 350 m at the target site (pH = 7.15) [60] were calculated by PHREEQC. These concentrations were set as the initial conditions within the domain (**Table 5**). The initial pore pressure at the depth of 350 m corresponds to the measured value at the equivalent depth in the boreholes installed at the target site [1]. The influence of the pre-existing fracture network in the rock was not considered. In the current work, the fracture initiation/propagation is considered only in the process of the cavity excavation; the generation of new fractures after the excavation is not considered. The parameters utilized in the calculation are summarized in **Table 6**. These parameter values were determined by referring to the literature [1, 19, 32, 34, 40, 41, 51, 61, 62, 63, and 64].

In the current work, the predictions were conducted for two different cases. One case, considering the THMC processes with pressure solution, is called the “PS condition” (including both pressure solution and free-face dissolution/precipitation in the mineral reactions). The other case, excluding the process of pressure solution, is called the “no-PS condition” (including only free-face dissolution/precipitation in the mineral reactions).

526 Changes in the distributions of the Ca and Si concentrations in the pore water around the disposal
527 cavity with time, predicted under the PS condition, are shown in **Fig. 15**. In the figure, the
528 concentrations of Ca and Si (c_{Ca} [mol/L] and c_{Si} [mol/L]) are shown by log notation (i.e., $\log_{10}c_{Ca}$ and
529 $\log_{10}c_{Si}$). This figure indicates that the concentrations of Ca and Si in the damaged zone increase over
530 time by the continuous supply of dissolved solutes due to the occurrence of pressure solution and free-
531 face dissolution within the fractures. Then, the solutes gradually diffuse from the damaged zone to the
532 intact rock zone. It should be noted that the predicted alternations in all solutes concentrations with
533 time, under the no-PS condition, show a little difference from those under the PS condition. This is
534 because the solute concentrations in the domain approach the equilibrium values in a relatively short
535 period, due to precipitation within the free-face, when additional dissolved solutes is supplied in pore
536 water due to pressure solution.

537 The changes in permeability with time around the disposal cavity under the no-PS and PS
538 conditions are shown in **Fig. 16.** In the figure, the permeability is shown by log notation (i.e., $\log_{10}k$).
539 The initial distribution of permeability depicted in the figure shows that the permeability in the
540 damaged zone, generated by the cavity excavation, increases to about two orders of magnitude greater
541 than the intact rock zone at the maximum. As is apparent from the figure, the permeability changes
542 the little with time under the no-PS condition, while the permeability in the damaged zone decreases
543 with time under the PS condition. The permeability in almost all the damaged zone eventually

544 decreases by about one order of magnitude after the disposal of the waste package. This is because of
545 the occurrence of pressure solution at the contacting asperities within the fractures in the damaged
546 zone.

547 In order to more quantitatively evaluate the permeability reduction within the damaged zone (D
548 > 0), due to pressure solution, the changes in permeability with time under the no-PS condition and
549 the PS condition at a specific observation point (Point 1, see **Fig. 17**) within the damaged zone are
550 shown in **Fig. 18**. It is apparent from the figure that, within the focused damaged zone, permeability
551 slightly increases with time due to free-face dissolution under the no-PS condition, while permeability
552 significantly decreases in the early stages of the analysis period under the PS condition. Afterwards, it
553 approaches the convergence value. For investigating the permeability reduction confirmed in **Fig. 18**,
554 changes in permeability within the first 10 years under the no-PS condition and the PS condition at
555 Point 1 are shown in **Fig. 17**. The figure shows that the permeability decreases by about one order of
556 magnitude within 5 years due to pressure solution.

557 As mentioned above, although the permeability decreases with time in almost all of the damaged
558 zone, due to the influence of pressure solution, the permeability in the tensile damage zone changes
559 little with time. A comparison of **Figs. 12** and **16** indicates that under the PS condition, the domain
560 where the permeability changes little within the damaged zone almost corresponds to the tensile
561 damage zone. This is because the pressure solution induced by the compressive stress does not occur

562 under the tensile stress condition. Thus, it is also important to investigate the failure mode of the
563 fractures in order to precisely predict the evolution of the rock permeability after the disposal of the
564 radioactive waste.
565

566 # 5 Conclusion

567 In this study, our coupled THMC model, denoted as *IPSACC*, was upgraded such that it can
568 describe the fracture evolution by incorporating the damage theory and the process of the mineral
569 dissolution/precipitation (i.e., pressure solution and free-face dissolution/precipitation) within the
570 generated fractures. The long-term evolution of the permeability in the porous rock within the
571 geological disposal system of high-level radioactive waste was predicted by the upgraded model. The
572 predictions for the excavation of the disposal cavity confirmed that the permeability within the
573 damaged zone, generated near the cavity during the excavation, increased to about two orders of
574 magnitude greater than that of the intact rock zone. The long-term coupled analysis after the disposal
575 of the radioactive waste showed that the permeability in almost all of the damaged zone, induced by
576 the shear mode, decreased by about one order of magnitude due to pressure solution at the contacting
577 asperities within the fractures. However, the permeability in the tensile damage zone changed little
578 from the initial state.

579 This work has focused on the process of the fracture initiation/propagation and the long-term
580 changes in permeability in the rock due to the mineral reactions. Therefore, the fracture
581 initiation/propagation is considered only in the process of the cavity excavation. Consequently, the
582 fracture initiation/propagation, due to the time-dependent deformation and the alternation of the stress
583 state, such as the thermal stress and creep after the disposal of the radioactive material, is not
584 considered and the actual fracture distribution within the rock may not be predicted precisely. Thus,
585 conducting numerical analyses that consider the time-dependent facture evolution is necessary.
586 Moreover, the proposed model only considers the geochemical effect due to the mineral
587 dissolution/precipitation for calculating the changes in rock permeability with time; and therefore, it
588 is necessary to consider the mechanical effects, such as the collapse of the grains and the elastic
589 deformation, in order to predict the changes in permeability more exactly. The proposed model
590 assumes that the rock stiffness does not recover with time after the fracture initiation/propagation, but
591 the healing of the rock stiffness may occur by an increase in the contact area within the fractures when
592 pressure solution is enhanced at the fracture contacts. Thus, updating the current model by taking into
593 account not only the fracture initiation/propagation, but also the recovery of the rock stiffness caused
594 by the mineral reactions, is required.
595

Acknowledgements

This work was supported by JSPS KAKENHI, subject nos. 18J12549 and 19H02237, and by the research grants funded by the Kajima Foundation and the Casio Science Promotion Foundation , Japan. Their support is gratefully acknowledged. The authors would like to thank all of the anonymous reviewers for their careful reading of our manuscript and their many insightful comments and suggestions. The data used in this work are available from the authors upon the request.

References

1. Aoyagi, K. and Ishii, E.: A Method for Estimating the Highest Potential Hydraulic Conductivity in the Excavation Damaged Zone in Mudstone. Rock Mech. Rock Eng. **52,** 385-401 (2019).

2. Zhang, C-H.: The stress-strain-permeability behaviour of clay rock during damage and recompaction. J. Rock Mech. Geotech. Eng. **8**, 16-26 (2016).

3. Tsang, C-F., Jing, L., Stephansson, O. and Kautsky, F.: The DECOVALEX III project: A summary of activities and-lessons learned. Int. J. Rock Mech. Min. Sci. **42**, 593-610 (2005).

4. Homand-Etienne, F. and Sebaibi, A.: Study of microcracking of the Lac du Bonnet granite. Eurock-ISRM Int. Symp. **2**, 1353-1362 (1996).

5. Souley, M., Homand, F., Peda, S. and Hoxha, D.: Damaged-induced permeability changes in granite: a case example at the URL in Canada. Int. J. Rock Mech. Min. Sci. **38**, 297-310 (2001).

6. Carlsson, SR. and Young, RP.: Acoustic emission and ultrasonic velocity study of excavated-induced microcrack damage at the underground research laboratory. Int. J. Rock Mech. Min. Sci. **30**, 901-907 (1993).

7. Kelsall, PC., Case, JB. and Chabanne, CR.: Evaluation of excavation induced changes in permeability. Int. J. Rock Mech. Min. Sci. **21**, 121-135 (1984).

8. Bauer, C., Homand, F. and Henry, JP.: In situ low permeability pulse test measurements. Int. J. Rock Mech. Min. Sci. **32**, 357-63 (1995).

9. Polak, A., Elsworth, D., Yasuhara, H., Grader, A. and Halleck, P.: Permeability reduction of a natural fracture

under net dissolution by hydrothermal fluids. Geophys. Res. Lett. **30** (20), 2020, doi:10.1029/2003 GL017575 (2003).

10. Polak, A., Elsworth, D., Yasuhara, H., Grader, AS. and Halleck, PM.: Spontaneous switching of permeability changes in a limestone fracture with net dissolution. Water Resour. Res. **40**, W03502, doi:10.1029/ 2003WR002717 (2004).

11. Yasuhara, H., Elsworth, D. and Polak, A.: Evolution of permeability in a natural fracture: the significant role of pressure solution. J. Geophys. Res. **109**, B03204, doi:10.1029/2003JB002663 (2004).

12. Yasuhara, H., Kinoshita, N., Ohfuji, H., Lee, DS., Nakashima, S. and Kishida, K.: Temporal alteration of fracture permeability in granite under hydrothermal conditions and its interpretation by coupled chemo-mechanical model. Appl. Geochem. **26**, 2074-2088 (2011).

13. Yasuhara, H. and Elsworth, D.: A numerical model simulating reactive transport and evolution of fracture permeability. Int. J. Numer. Anal. Methods Geomech. **30**, 1039-1062 (2006).

14. Rutqvist, J., Wu, Y-S., Tsang, C-F. and Bodvasson, G.: A modeling approach for analysis of coupled multiphase fluid flow, heat transfer, and deformation in fractured porous rock. Int. J. Rock Mech. Min. Sci. **39**, 429-442 (2002).

15. Suzuki, H., Nakama, S., Fujita, T., Imai, H. and Sazarshi, M.: A long-term THMC assessment on the geochemical behavior of the bentonite buffer. J. Nucl Fuel Cycle. Environ, **19**, 39-50 (2012).

16. Nasir, O., Fall, M. and Evgin, E.: A simulator for modeling of porosity and permeability changes in near field sedimentary host rocks for nuclear waste under climate changes influences. Tunneling and Underground Space

Technology. **42**, 122-135 (2014).

17. Fall, M., Nasir, O. and Nguyen, T. S.: A coupled hydro-mechanical model for simulation of gas migration in host sedimentary rocks for waste repositories. Eng. Geol. **176**, 24-44 (2014).

18. Zhang, R., Yin, X., Winterfeld, P. H. and Wu, Y.-S.: A fully coupled thermal-hydrological-chemical model for CO_2 geological sequestration. J. Nat. Gas Sci. Eng. **28**, 280-304 (2016).

19. Ogata, S., Yasuhara, H., Kinoshita, N., Cheon, DS. and Kishida, K.: Modeling of coupled thermal-hydraulic-mechanical-chemical process for predicting the evolution in permeability and reactive transport behavior within single rock fractures., Int. J. Rock Mech. Min. Sci. **107**, 271-281 (2018).

20. Wei, CH., Zhu, WC. Chen, S. and Ranjith, PG.: A coupled thermal-hydrological-mechanical damage model and its numerical simulations of damage evolution in APSE. Materials. **9**, 841, doi: 10.3390/ma9110841 (2016).

21. Li, LC., Tang, CA., Wang, SY. and Yu, J.: A coupled thermo-hydrologic-mechanical damage model and associated application in a stability analysis on a rock pillar. Tunneling and Underground Space Technology. **34**, 38-53 (2013).

22. Wei, CH., Zhu, WC., Yu, QL., Xu, T. and Jeon, S.: Numerical simulation of excavation damaged zone under coupled thermal-mechanical conditions with varying mechanical parameters. Int. J. Rock Mech. Min. Sci. **75**, 169-181 (2015).

23. Xu, T., Zhou, GL., Heap, J-M., Zhu, WC., Chen, CF. and Boud, P.: The influence of temperature on time-dependent deformation and failure in granite: a mesoscale modeling approach. Rock Mech. Rock Eng. doi: 10.1107/ s00603-0.17-1228-9 (2017).

24. Poulet, T., Karrech, A., Lieb, RK., Fisher, L. and Schaubs, P.: Thermal-hydraulic-mechanical-chemical coupling with damage mechanics using ESCRIPTRT and ABAQUAS. Tectonophysics. 124-132 (2013).

25. Marschall, P., Giger, S., Vassiere, DLR., Shao, H., Leung, H., Nussbaum, C., Trick, T., Lanyon, B., Senger, R., Lisjak, A. and Alcolea, A.: Hydro-mechanical evolution of the EDZ as transport path for radionuclides and gas: insights from the Mont Terri rock laboratory (Switzerland). Swiss J. Geosci. **110**, 173-194 (2017).

26. Lang, PS., Paluszny, A. and Zimmerman, RW.: Hydraulic sealing due to pressure solution contact zone growth in siliciclastic rock fractures. J. Geophys**.** Res. Solid Earth. **120**, 4080-4101(2015).

27. Taron, J., Elsworth, D. and Min., KB.: Numerical simulation of thermal-hydrologic-mechanical-chemical processes in deformable fractured porous media. Int. J. Rock Mech. Min. Sci. **46**, 842-854 (2009).

28. Weitao, L., Jiyuan, Z., Ruiai, N., Yifan, Z, Baichao, X. and Xi, S.: A Full Coupled Thermal-Hydraulic-Chemical Model for Heterogeneity Rock Damage and Its Application in Predicting Water Inrush. Appl. Sci. 9, 2195; doi:10.3390/app9112195 (2019).

29. Chaojun, F., Mingkun, L., Sheng, L., Haohao, Z., Zheng, Y. and Zheng, L.: A Thermo-Hydro-Mechanical-Chemical Coupling Model and Its application in Acid Fracturing Enhanced Coalbed Methane Recovery Simulation. Energies. 12, 626; doi:10.3390/en12040626 (2019).

30. Tang, CA.: Numerical simulation on progressive failure leading to collapse and associated seismicity. Int. J. Rock Mech. Min. Sci. **34**, 249-262 (1997).

31. Tang, CA., Liu, H., Lee, KKP., Tsui, Y. and Tham, LG.: Numerical studies of the influence of microstructure on

684 rock failure in uniaxial compression- Part I : effect of heterogeneity. Int. J. Rock Mech. Min. Sci. **37**, 555-569
685 (2000).
686 32. Zhu, WC. and Tang, CA.: Micromechanical model for simulating the fracture process of rock. Rock Mech. Rock
687 Eng. **37**, 25-56 (2004).
688 33. Li, G. and Tang, CA.: A statistical meso-damage mechanical method for modeling trans-scale progressive failure
689 process of rock. Int. J. Rock Mech. Min. Sci. **74**, 133-150 (2015).
690 34. Liu, HY., Roquete, M., Kou, SQ. and Lindqvist, PA.: Characterization of rock heterogeneity and numerical
691 verification. Eng. Geol. **72**, 89-119 (2004).
692 35. Wang, SY., Sloan, SW., Scheng, DC., Yang, SQ. and Tang, CA.: Numerical study of failure behavior of pre-
693 cracked rock specimens under conventional triaxial compression. Int. J. Solids Struct. **51**, 1132-1148 (2014).
694 36. Weibull, W.: A statistical distribution function of wade applicability. J. Appl. Mech. **18**, 293-297 (1951).
695 37. Zhu, WC., Weu, C., Li, S., Wei, J. and Zhang, M.: Numerical modeling on destress blasting in coal seam for
696 enhancing gas drainage, Int. J. Rock Mech. Min. Sci. **59**, 179-190 (2013).
697 38. Zimmerman, R W.: Thermal conductivity of fluid-saturated rocks. J. Petrol. Sci. Eng. **3**, 219-227 (1989).
698 39. Hashin, Z. and Shtrikman, H.: A variational approach to theory of the effective magnetic permeability of
699 multiphase materials. J. Appl. Phys. **33**, 3125-3131 (1962).
700 40. Vosteen, HD. And Schellschmidt.: Influence of temperature on thermal conductivity, capacity and thermal
701 diffusivity of different types of rock. Phys. Chem. Earth. **28**, 499-509 (2003).

41. Revil, A.: Pervasive pressure-solution transfer: a poro-visco-plastic model. Geophys. Res. Lett. **26**, 255-258 (1999).

42. Tada, R. and Silver T.: A new mechanism for pressure solution in porous quartzose sandstone. Geochemi. Cosmochim. Acta. **51**, 2295-2301 (1987).

43. Cocks, A. and Ashby, M.: Intergranular fracture during power-law creep under multiaxial stresses. Metal Science. **14**, 395-402 (1980).

44. COMSOL2014：COMSOL MULTIPHYSICS. Version 5.0, Available from www.comsol.com (2004).

45. Parkhurst, DL. and Appelo, CAJ.: Description of Input and Examples for PHREEQC Version3-A Computer Program for Speciation, Batch-Reaction, One-Dimensional Transport, and Inverse Geochemical Calculations, Online version availableromhttp://wwwbrr.cr.usgs.gov/projects/GWC_coupled/phreeqc/phreeqc3-html/phreeq-c3.htm.

46. Azad, Vj., Li, C., Verba, C., ldeker, JH. and lsgor, OB.: A COMSOL-GEMS interface for modeling coupled reactive-transport geochemical processes. Comput. Geosci-UK. **92**, 79-89 (2016).

47. Coussy, O.: Poromechanics. John Willey & Sons, Chinese, England (2004).

48. Nardi, A., Idiart, a., Trincheo, P., Vries, LM. And Molinero, J.: Interface COMSOL-PHREEQC (iCP), an efficient framework for the solution of coupled multiphysics and geochemistry. Comput. Geosci. **69**, 10-21 (2014).

49. Japan Nuclear Cycle Development Institute, 2000: Second Progress Report on Research and Development for the Geological Disposal of HLW in Japan, Supporting Report 2 Repository Design and Engineering Technology, H12:

720 Project to Establish the Scientific and Technical Basis for HLW Disposal in Japan. JNC TN1410 2000-003, IV-
721 139-IV-160 (2000) (in Japanese).
722 50. JNC (Japan Nuclear Cycle Development Institute), 2005: Development and management of the technical
723 knowledge base for the geological disposal of HLW, Summary of the H17 project reports, Vol. 1. Scientific
724 research of deep underground. JNC TN1400 2005-014 (2005) (in Japanese).
725 51. Matsumura, S., Sirato, N. and Taki, H.: Evaluation of stability of gallery of underground facility for Horobe
726 Underground Research Laboratory Project. The 58th Japan Society of Civil Engineering Symposium (2003).
727 52. Aoyagi, K., Tsusaka, K., Tokiwa, T., Kondo, K., Inagaki, D. and Kato, H.: A study of the regional stress and the
728 stress state in the galleries of the Horonobe Underground Research Laboratory. In: Proceedings of the 6th
729 International Symposium on In-Situ Rock Stress. Sendai. Japan. 331–338 (2013).
730 53. Tachi, Y., Yothuji, K., Seida, Y. and Yui M.: Diffusion and sorption of Cs^+, I^- and HTO in samples of the
731 argillaceous Wakkanai Formation from the Horonobe URL, Japan: Clay-based modeling approach. Geochim.
732 Cosmochim. Acta. **75**, 6742-6759 (2011).
733 54. Tester, JW., Worley, WG., Robinson, BA., Grigsby, CO. Feerer, JL.: Correlating quartz dissolution kinetics in pure
734 water from 25 to 625°C. Geochim. Cosmochim. Acta.**58**, 2407–2420 (1994).
735 55. Helgeson, HC., Murphy, WM. and Aagaard, P.: Thermodynamic and kinetic constraints on reaction rates among
736 minerals and aqueous solutions. II. Rate constants, effective surface area, and the hydrolysis of feldspar. Geochim.
737 Cosmochim. Acta. **48**, 2405–2432 (1984).

738 56. Chou, L. and Wollast, R.: Study of weathering of albite at room temperature and pressure with a fluidized bed
739 reactor. Geochem. Cosmochim. Acta. **48**, 2205–2217 (1984).
740 57. Hellman, R.: The albite-water system: part I. The kinetics of dissolution as a function of pH at 100, 200, and 300C.
741 Geochim. Cosmochim. Acta. **58**, 595–611 (1994).
742 58. Oelkers, EH. and Schott, J.: Experimental study of anorthite dissolution and the relative mechanism of feldspar
743 hydrolysis. Geochim. Cosmochim. Acta. **59**, 5039–5053 (1995).
744 59. Palandri, JL. and Kharaka, YK.: A compilation of rate parameters of mineral-water interaction kinetics for
745 application to geochemical modelling. US Geological Survey open file report. 2004–1068 (2204).
746 60. Miyakawa, K., Mezawa, T., Mochizuki, A. and Sasamoto, H.: Data of Ground Chemistry Obtained in the
747 Horonobe Underground Research Laboratory Project (Fy2014-2016). JAEA-Data/Code (2017).
748 61. Ota, K., Abe, H., Yamaguchi, T., Kunimaru, T., Ishi, E., Kurilami, H., Tomura, G., Shibano, K., Hma, K., Matsui
749 H., Niizato, T., Tkahashi, K., Niunoya, S, Ohara, H., Asamori, K., Morioka, H., Shigeta, N. and Fushima, T.:
750 Horonobe Underground Research Laboratory Project Synthesis of Phase I Investigations 2001-2005. JAEA-
751 Research. 2007-044 (2007).
752 62. Yamamoto, T., Masui, H., Horiuchi, Y. and Tominaga, E.: THERMAL PROPERTIES ON SOFT SEDIMENTARY
753 ROCK OF HORONOBE UNDERGROUND RESEARCH PROGRAM. The 14th Rock Mechanics Symposium in
754 JAPAN (2005).
755 63. Miyazawa, D., Sanada, H., Kiyama, T., Sugita, Y. and Ishijima, Y.: Proelastic coefficients for siliceous rocks

distributed in the Horonobe area, Hokkaido, Japan. J MMIJ. **127**, 132–138 (2011).

64. Wang, J., Elsworth, D., Wu, Yu., Liu, J., Zhu W. and Liu, Y.: The Influence of Fracturing Processes: A Comparison Between Water, Oil and SC-CO^2. Rock. Mech. Rock. Eng. DOI 10.1007/s00603-017-1326-8 (2017).

65. Anbeek, C.: Surface roughness of mineral sand implications for dissolution studies. Geochim. Cosmochim. Acta. **56,** 1461–1469 (1992).

Tables and Figures

Tables

Table 1 Parameters used in benchmark simulation of coupled THM problem.

Table 2 Chemical conditions (compositions of aqueous species/minerals and pH) of calculation domain at initial state and inlet boundary for benchmark simulation of 1D reactive transport problem.

Table 3 Settings of mineral composition (volumetric ratios of minerals) used in simulation.

Table 4 Parameters of kinetic dissolution rate constants for minerals.

Table 5 Initial pore water composition used in simulation.

Table 6 Parameters used in simulation.

Figures

Fig. 1 THMC interactions considered in the proposed model. The interactions expressed as gray arrows were not considered in our previous model [19], while the ones expressed as white arrows were taken into account.

Fig. 2 Constitutive law of elastic damage theory under uniaxial tensile stress and uniaxial compressive stress (illustrated in Wei et al., 2015) [22].

Fig. 3 Conceptualization of mesoscopic fractures.

Fig. 4 Geometrical model that includes representative element in rock fracture area [11].

Fig. 5 Calculation procedure of proposed model.

Fig. 6 Description of benchmark simulation (thermal pressurization problem).

Fig. 7 Comparisons of results by proposed model versus analytical solution for non-dimensional temperature and non-dimensional pore pressure at different depth and at various times (t = 1.0 ×10^6, 5.0 ×10^6, and 1.0 ×10^7.

Fig. 8 Description of benchmark simulation of 1D reactive transport problem.

Fig. 9 Comparisons of results by proposed model versus PHREEQC solutions for evolution in concentrations of (a) Al and (b) K.

Fig. 10 Calculation domain of long-term coupled THMC simulation.

Fig. 11 Description of excavation analysis.

Fig. 12 Evolution of damaged zone during cavity excavation.

Fig. 13 Temperature depending on time T_b (t) used as boundary condition applied on periphery of cavity [49].

Fig. 14 Description of long-term coupled THMC analysis.

Fig. 15 Changes in distribution of solute concentrations with time under PS condition: (a) Ca concentrations and (b) Si concentrations.

Fig. 16 Changes in permeability with time under (a) no-PS condition and (b) PS condition.

Fig. 17 Specific observation points close to cavity. The damaged zone is obtained after the completion of the excavation analysis. Point 1 is set within the predicted damaged zone.

Fig. 18 Changes in permeability with time under no-PS condition and PS condition at observation point (Point 1) within damaged zone shown in **Fig. 17**.

Fig. 19 Changes in permeability within first 10 years under no-PS condition and PS condition at observation point (Point 1) within damaged zone shown in **Fig. 17**.

Table 1 Parameters used in benchmark simulation of coupled THM problem.

Parameter	Value
Young's modulus [Pa] E	6.0×10^{5}
Porosity [-] ϕ	0.40
Poisson's ratio [-] v	0.30
Fluid dynamic viscosity [Pa s] μ	1.0×10^{-3}
Permeability [m^2] k	9.20×10^{-17}
Thermal expansion coefficient of solid [K^{-1}] α_T	6.20×10^{-6}
Equilibrium volumetric heat capacity [kJ m^{-3} K^{-1}] $(\rho C_p)_{eq}$	2.70×10^{3}
Equilibrium thermal conductivity [Wm^{-1} K^{-1}] λ_{eq}	0.50
Biot's coefficient [-] α_B	1.0
Storage coefficient [Pa^{-1}] S	1.1×10^{-10}

Table 2 Chemical conditions (compositions of aqueous species/minerals and pH) of calculation domain at initial state and inlet boundary for benchmark simulation of 1D reactive transport problem.

Chemical conditions: compositions of aqueous species/minerals and pH	Initial state	Inlet boundary
Al [mol/L]	5.11×10^{-9}	1.00×10^{-8}
Br [mol/L]	1.75×10^{-5}	0
C [mol/L]	4.94×10^{-3}	1.90×10^{-4}
Ca [mol/L]	1.40×10^{-3}	3.04×10^{-4}
Cl [mol/L]	1.10×10^{-2}	9.03×10^{-4}
F [mol/L]	$3.16\times10^{--5}$	1.60×10^{-5}
Fe [mol/L]	7.18×10^{-6}	5.37×10^{-5}
K [mol/L]	2.50×10^{-4}	7.16×10^{-4}
Mn [mol/L]	3.46×10^{-6}	0
Mg [mol/L]	7.40×10^{-4}	1.99×10^{-4}
Na [mol/L]	1.31×10^{-2}	3.04×10^{-4}
P [mol/L]	3.87×10^{-6}	0
S [mol/L]	9.59×10^{-4}	4.80×10^{-4}
Si [mol/L]	1.99×10^{-4}	2.50×10^{-6}
Sr [mol/L]	0	6.84×10^{-7}
pH [-]	7.52	7.30
Calcite [mol/L]	6.065	-
K-feldspar [mol/L]	0.239	-
Albite [mol/L]	0.289	-
Illite [mol/L]	0.144	-
Pyrite [mol/L]	1.17	-

Table 3 Settings of mineral composition (volumetric ratios of minerals) used in simulation.

Mineral composition	Volumetric ratio χ_j
Quartz	0.16
K-feldspar	0.05
Albite	0.06
Anorthite	0.02
Smectite	0.26
Cristobalite	0.45

Table 4 Parameters of kinetic dissolution rate constants for minerals.

Mineral	Molar volume $V_{m,j}$ [m^3 mol^{-1}]	Pre-exponential factor $k^0_{+,j}$ [mol m^{-2} s^{-1}]	Activation Energy $E^0_{+,j}$ [kJ mol^{-1}]
Quartz	2.27×10^{-5}	276 [55]	90 [55]
K-feldspar	1.09×10^{-4}	1.28×10^{-5} [56]	38.0 [56]
Albite	1.00×10^{-4}	3.91×10^{-4} [57, 58]	50.7 [57, 58]
Anorthite	1.01×10^{-4}	9.97×10^{-7} [59]	17.8 [59]
Smectite	1.40×10^{-4}	4.64×10^{-5} [60]	49.4 [60]
Cristobalite	2.57×10^{-5}	1.20×10^{-1} [61]	65.0 [61]

Table 5 Initial pore water composition used in simulation.

Initial pore water composition	Value
Al [mol L^{-1}]	1.7×10^{-3}
Ca [mol L^{-1}]	8.6×10^{-7}
K [mol L^{-1}]	7.9×10^{-6}
Na [mol L^{-1}]	1.6×10^{-3}
Si [mol L^{-1}]	2.2×10^{-4}
Mg [mol L^{-1}]	1.8×10^{-7}
Fe [mol L^{-1}]	1.1×10^{-7}
pH	7.15 [60]

959
960
961
962
963

964 **Table 6** Parameters used in simulation.

Parameter	Value
Homogeneity index of material properties [-] m	3.0 [32, 34]
Characteristic value of elastic modulus [GPa] $E_0{}^s$	1.82 [1]
Characteristic value of uniaxial tensile strength [MPa] $f_{t0}{}^s$	1.83 [1]
Characteristic value of uniaxial compressive strength [MPa] $f_{c0}{}^s$	15.4 [1]
Internal friction angle [°] θ	30.0 [51]
Poisson's ratio [-] v	0.17 [1]
Initial permeability [m^2] k_0	2.88×10^{-16} [61]
Porosity [-] ϕ	0.416 [1]
Initial thermal conductivity of the solid [w m^{-1} K^{-1}] λ_{m0}	0.75 [62]
Heat capacity of the solid [kJ kg^{-1} K^{-1}] $C_{p,m}$	0.8 [62]
Empirical constant [-] C_a	0.0034 [41]
Empirical constant [-] C_b	0.0039 [41]
Biot-Willis coefficient [-] α_B	0.92 [63]
Storage coefficient [Pa^{-1}] S	2.85×10^{-10} [63]
Coefficient that represents the damage-permeability effect [-] α_k	5.0 [64]
Thermal expansion coefficient of solid [K^{-1}] α_T	1.15×10^{-5} [62]
Roughness factor [-] f_r	6.75 [19]
Critical stress [MPa] σ_c	15.0 [19]
Pre-exponential factor of diffusion of solute [m^2 s^{-1}] D_b^0	5.2×10^{-8} [41]
Activation energy of diffusion of solute [kJ mol^{-1}] E_D	13.5 [41]
Constant [-] a	0.07 [19]

965
966
967
968
969
970

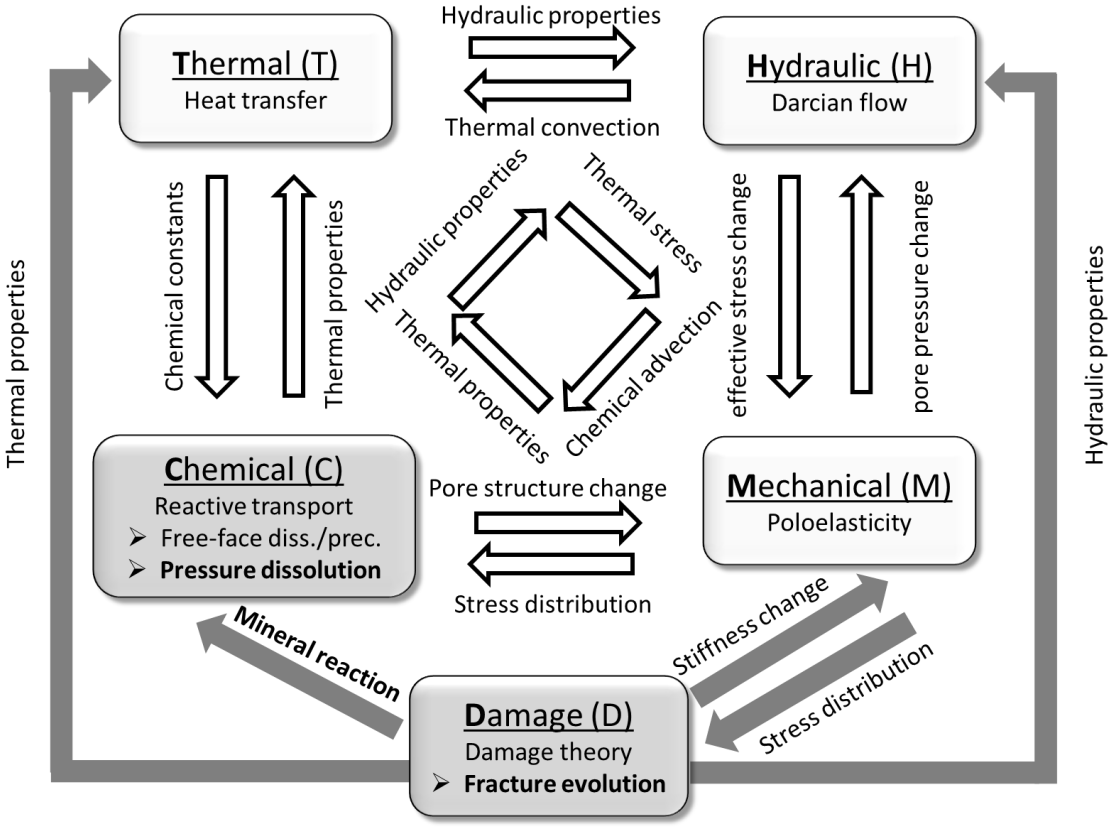

971

972 **Fig. 1** THMC interactions considered in the proposed model. The interactions expressed as gray
973 arrows were not considered in our previous model [19], while the ones expressed as white arrows were
974 taken into account.

975

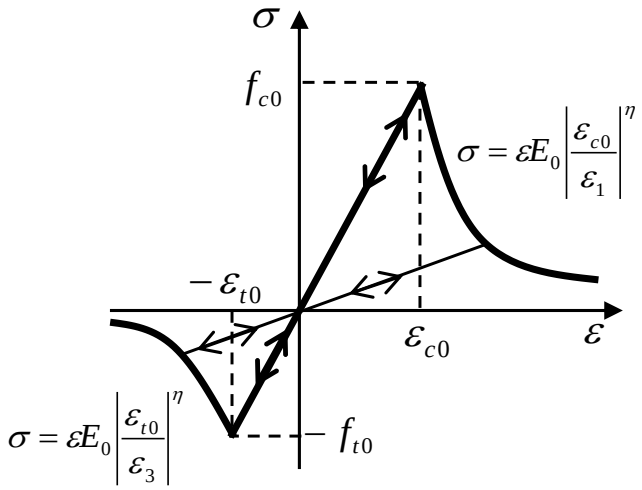

976

977 **Fig. 2** Constitutive law of elastic damage theory under uniaxial tensile stress and uniaxial
978 compressive stress (illustrated in Wei et al., 2015 [22]).

979

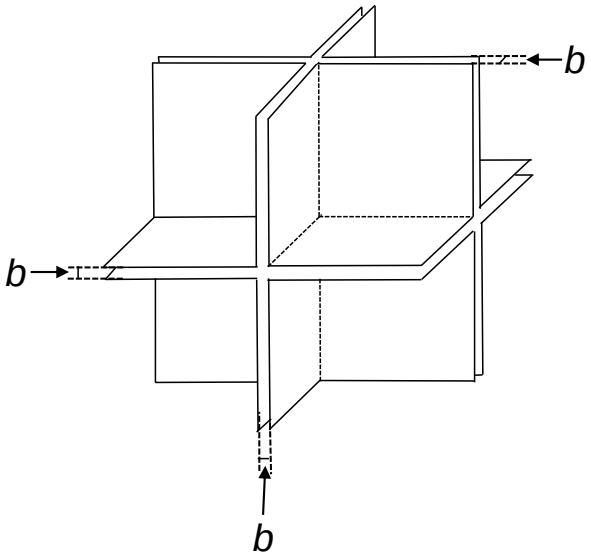

Fig. 3 Conceptualization of mesoscopic fractures.

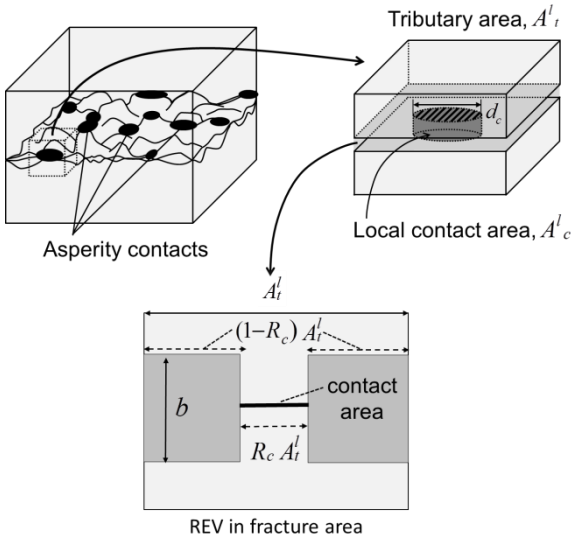

998

999 **Fig. 4** Geometrical model that includes representative element in rock fracture area [11].

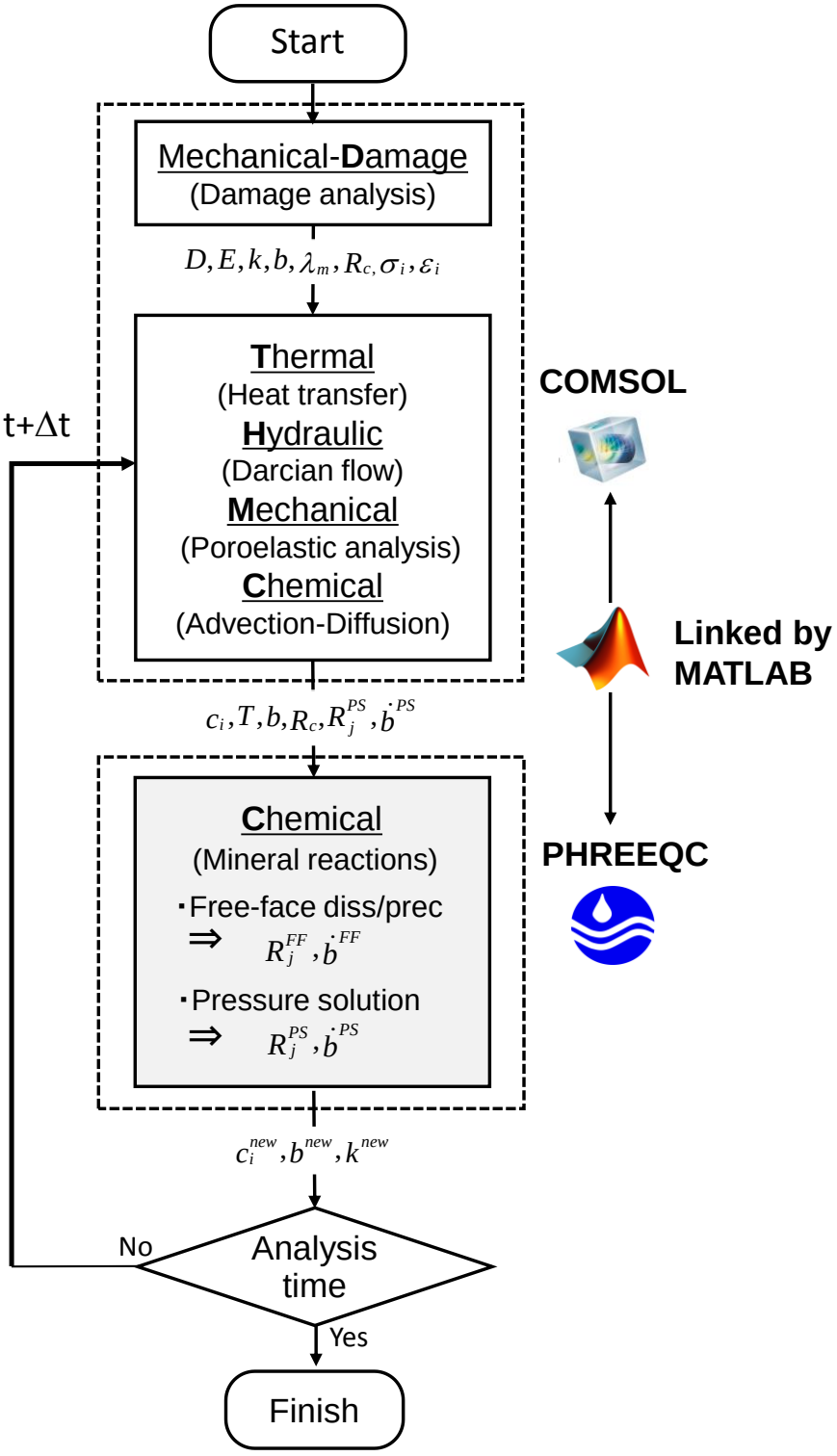

Fig. 5 Calculation procedure of proposed model.

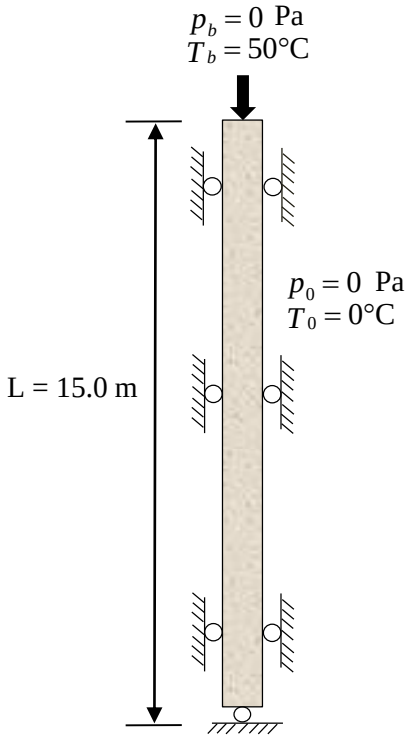

Fig. 6 Description of benchmark simulation (thermal pressurization problem).

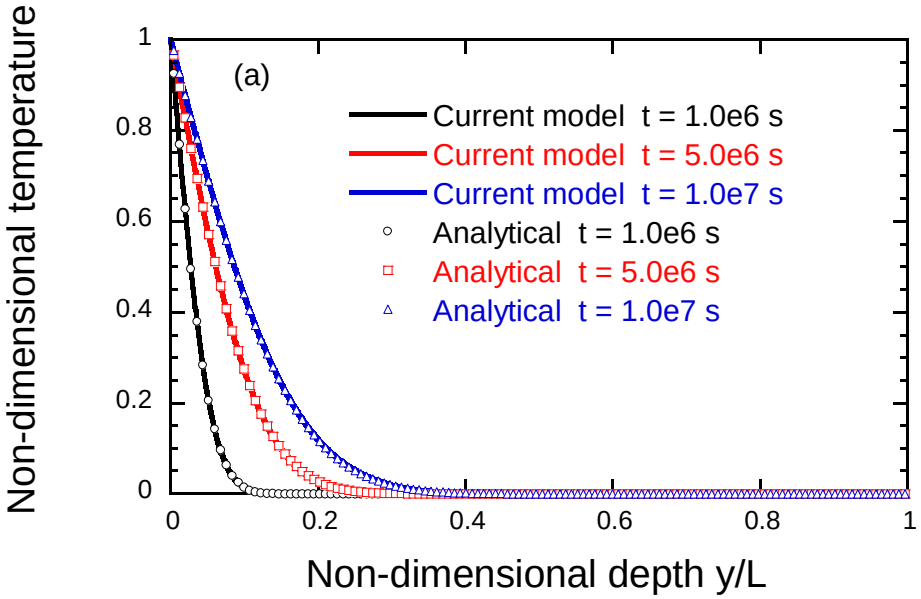

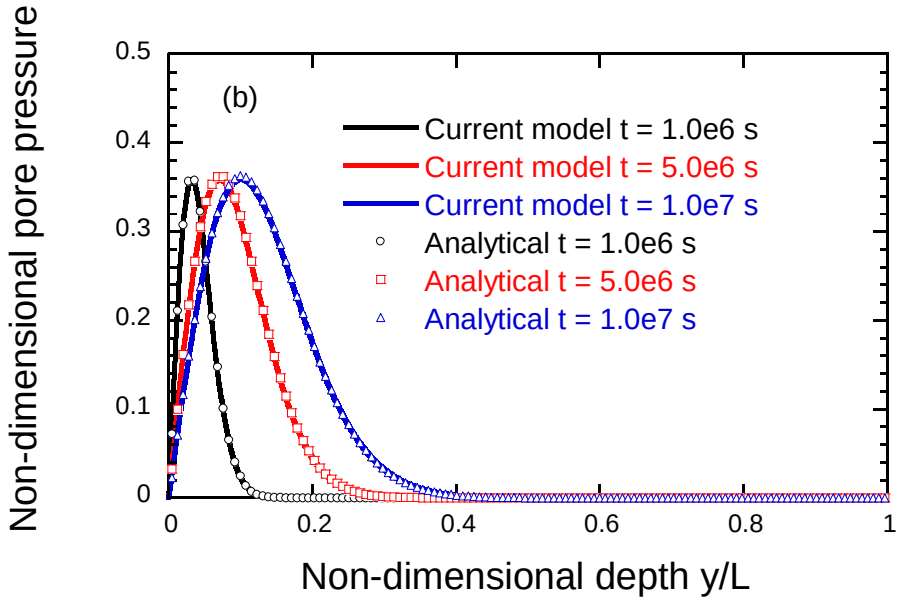

Fig. 7 Comparisons of results by proposed model versus analytical solution for (a) non-dimensional temperature and (b) non-dimensional pore pressure at different depths and at various times (t = 1.0 $\times 10^6$, 5.0 $\times 10^6$, and 1.0 $\times 10^7$.

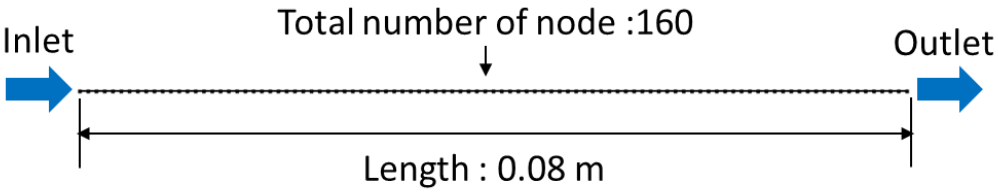

Fig. 8 Description of benchmark simulation of 1D reactive transport problem.

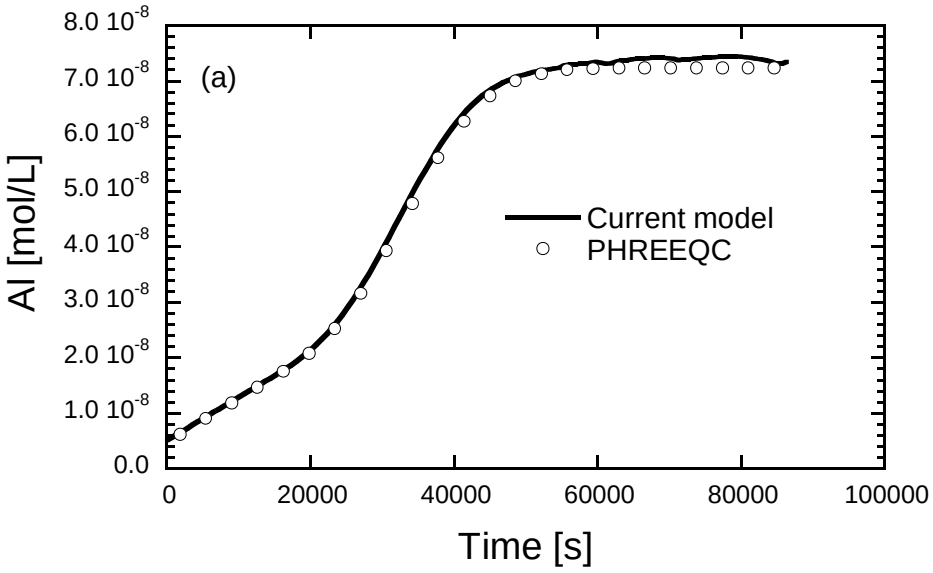

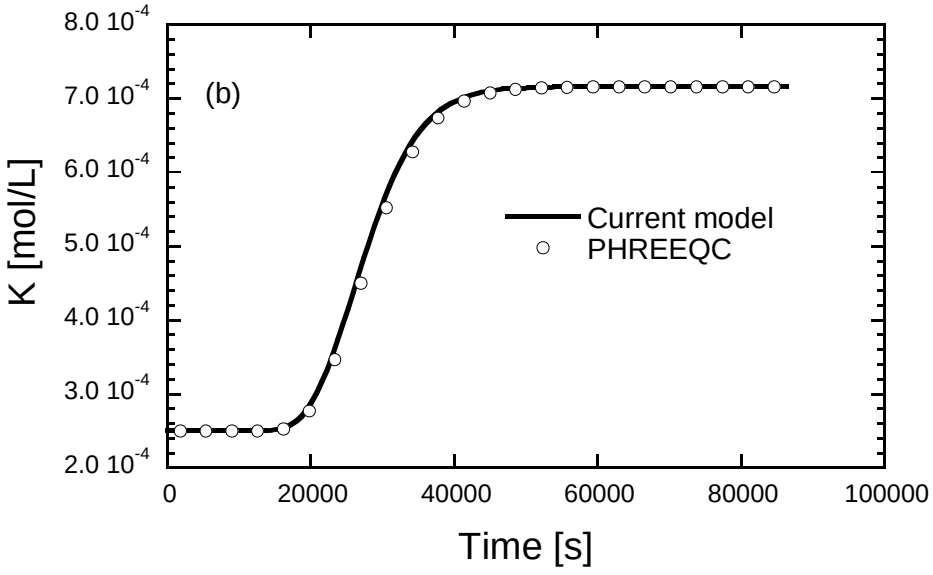

Fig. 9 Comparisons of results by proposed model versus PHREEQC solutions for evolution in concentrations of (a) Al and (b) K.

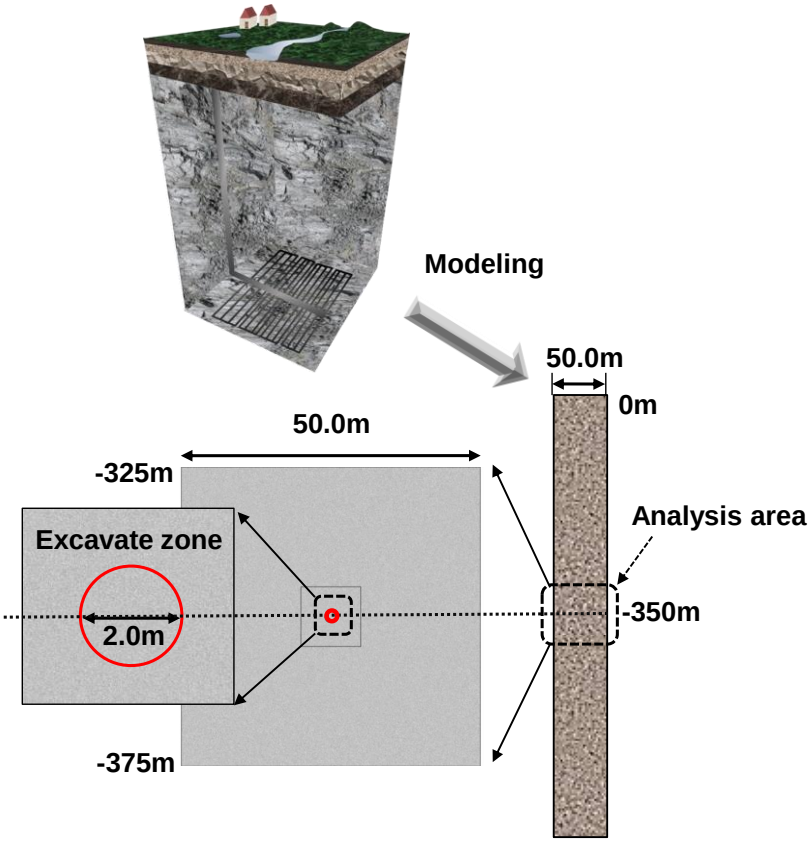

Fig. 10 Calculation domain of long-term coupled THMC simulation.

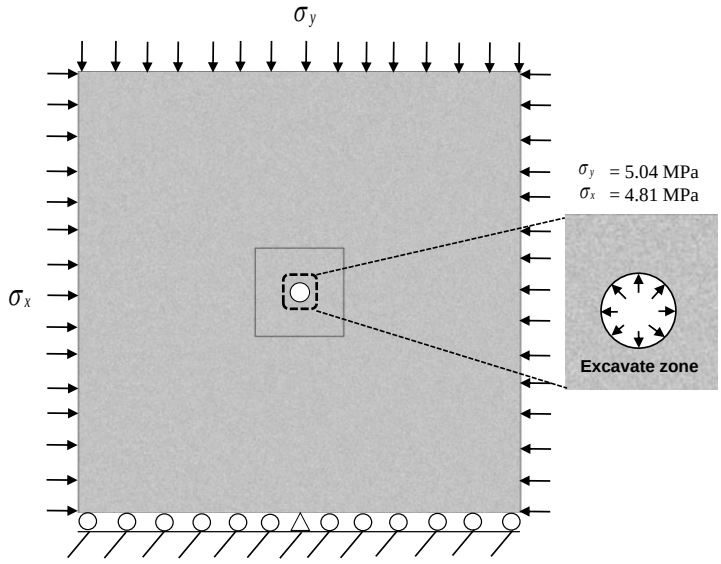

Fig. 11 Description of excavation analysis.

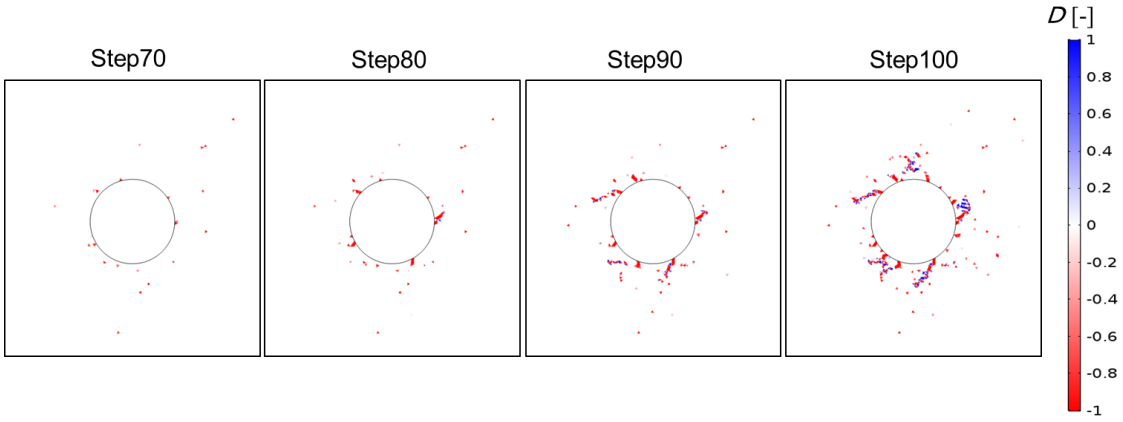

Fig. 12 Evolution of damaged zone during cavity excavation.

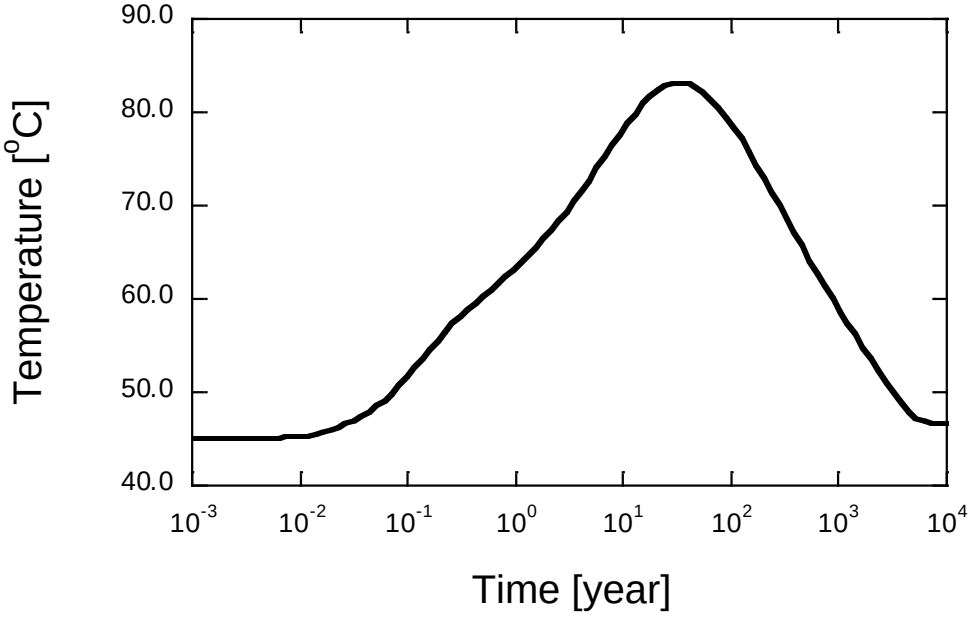

Fig. 13 Temperature depending on time T_b (t) used as boundary condition applied on periphery of cavity [49].

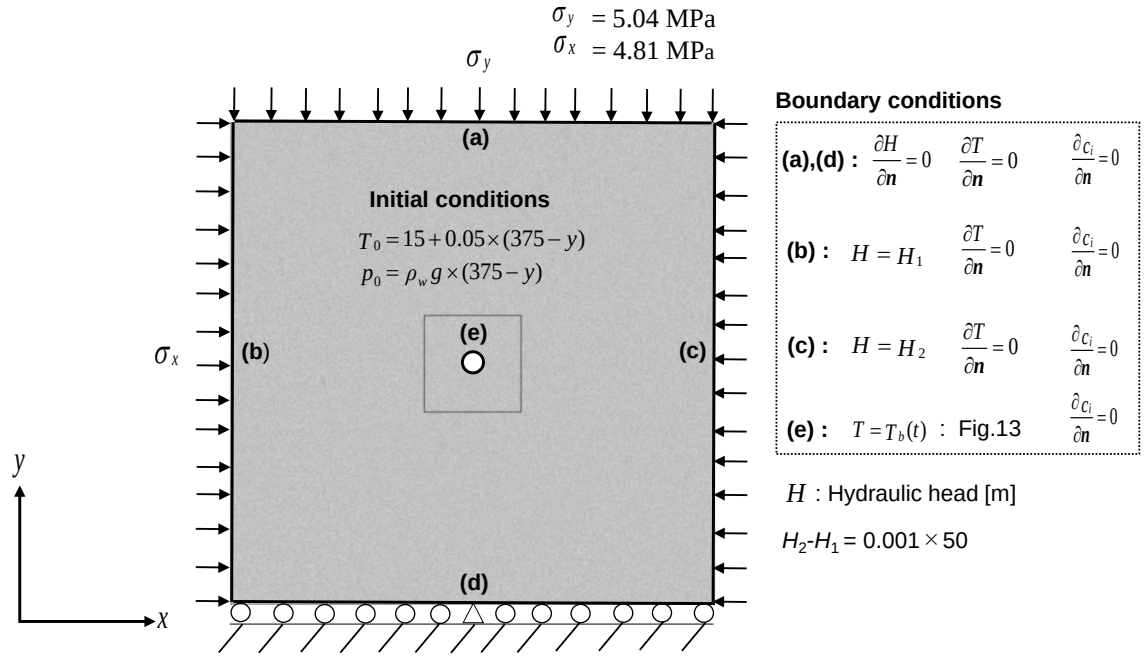

Fig. 14 Description of long-term coupled THMC analysis.

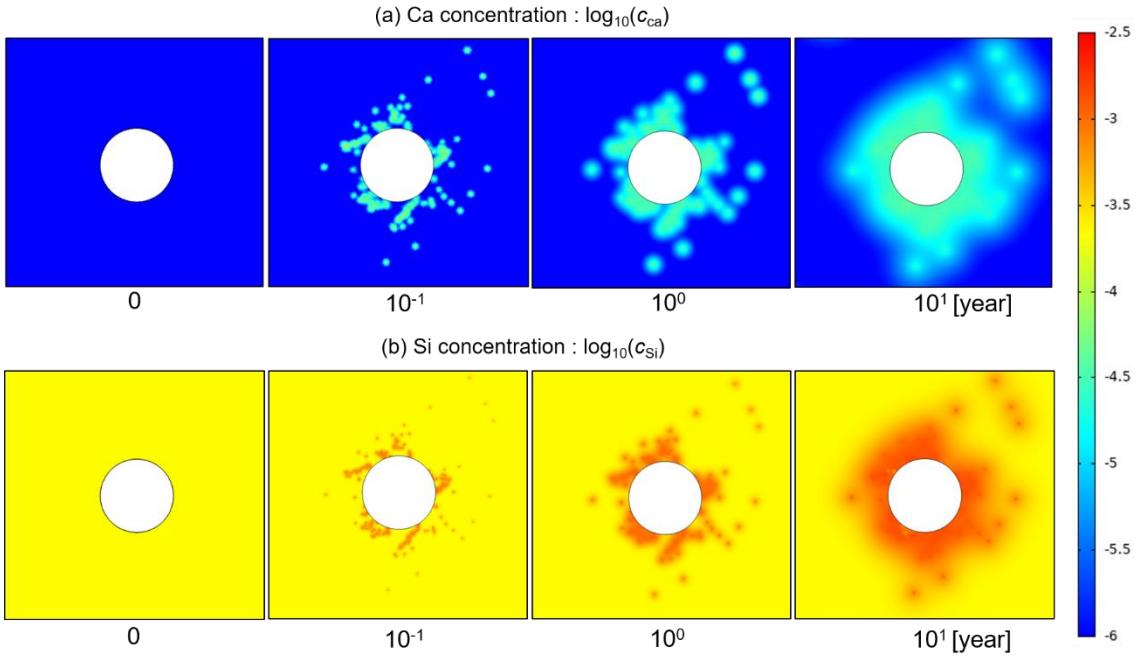

Fig. 15 Changes in distribution of solute concentrations with time under PS conditions: (a) Ca concentrations and (b) Si concentrations.

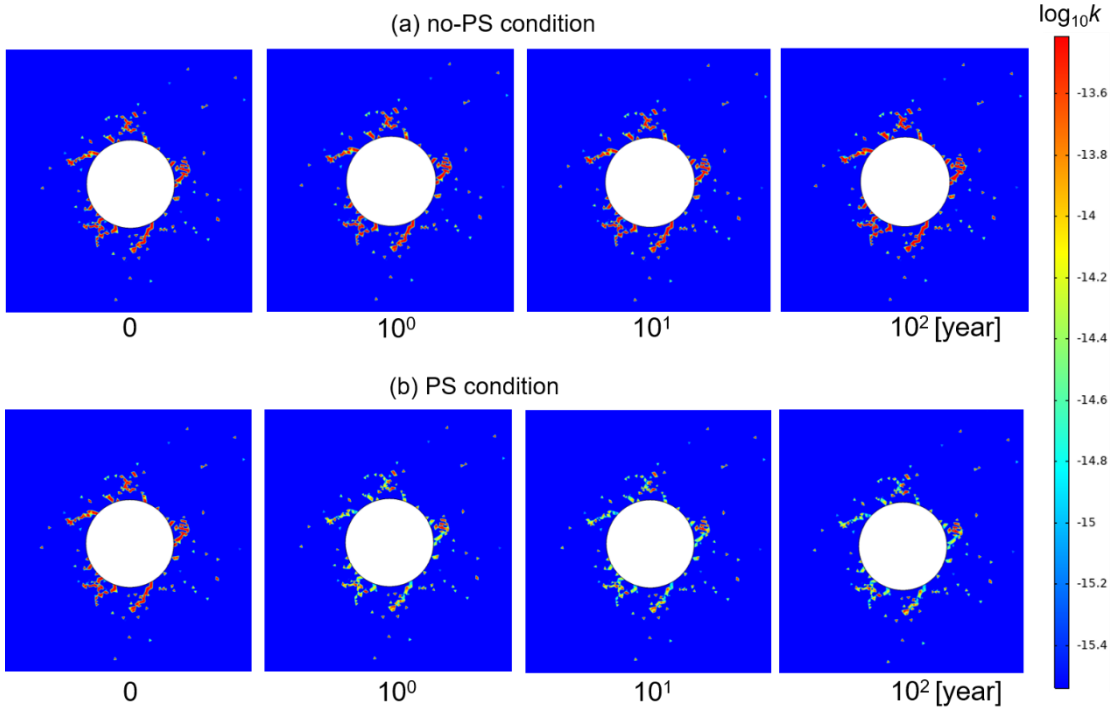

Fig. 16 Changes in permeability with time under (a) no-PS condition and (b) PS condition.

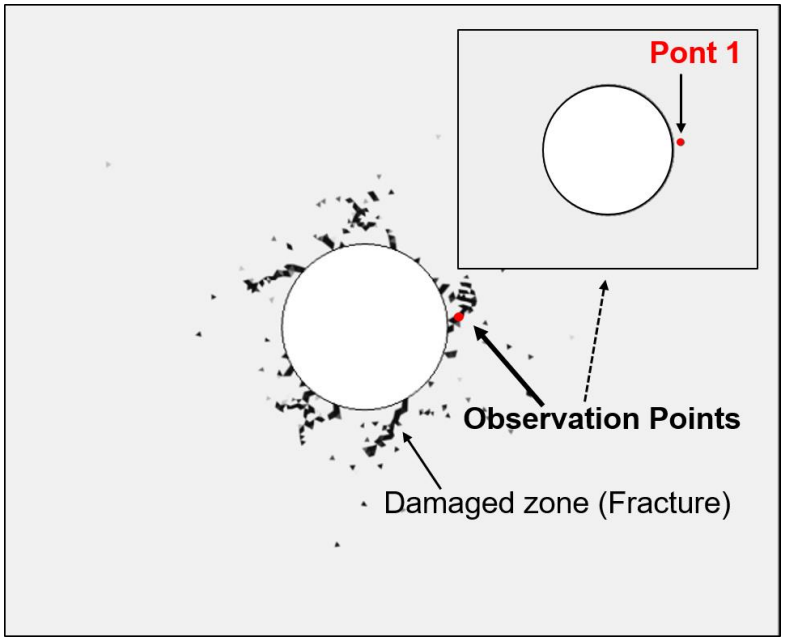

Fig. 17 Specific observation points close to cavity. The damaged zone is obtained after the completion of the excavation analysis. Point 1 is set within the predicted damaged zone.

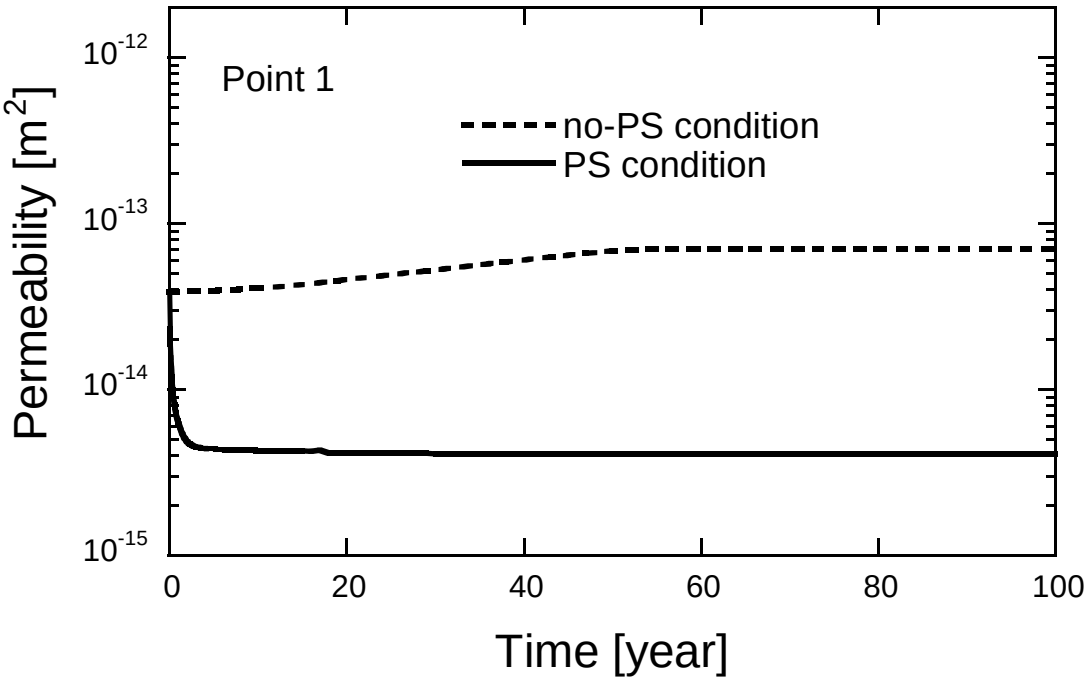

Fig. 18 Changes in permeability with time under no-PS condition and PS condition at observation point (Point 1) within damaged zone shown in **Fig. 17**.

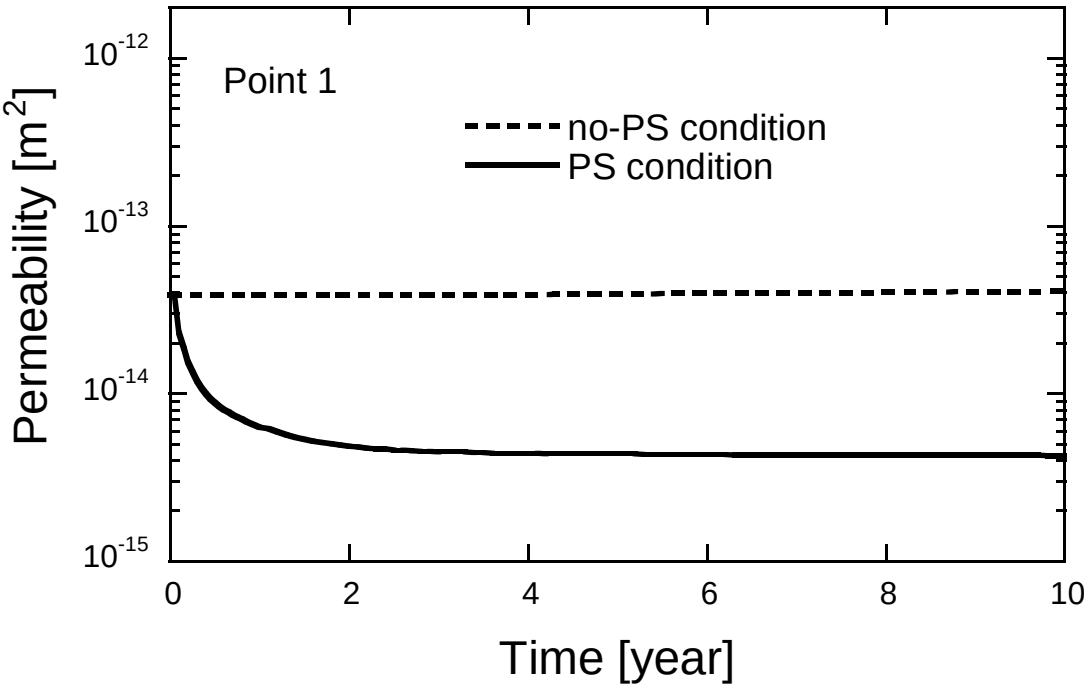

1111

1112 **Fig. 19** Changes in permeability within first 10 years under no-PS condition and PS condition at observation

1113 point (Point 1) within damaged zone shown in **Fig. 17**.

1114

Reply to Reviewer2's comments

Click here to view linked References

Reply to Reviewer3's comments

Click here to view linked References